



Contents lists available at ScienceDirect

## Journal of Materials Science &amp; Technology

journal homepage: [www.elsevier.com/locate/jmst](http://www.elsevier.com/locate/jmst)

## Research Article

## Small-scale analysis of brittle-to-ductile transition behavior in pure tungsten

Yeonju Oh<sup>a</sup>, Won-Seok Ko<sup>b</sup>, Nojun Kwak<sup>a</sup>, Jae-il Jang<sup>c</sup>, Takahito Ohmura<sup>d,\*</sup>, Heung Nam Han<sup>a,\*\*</sup><sup>a</sup> Department of Materials Science and Engineering & Research Institute of Advanced Materials, Seoul National University, Seoul 08826, South Korea<sup>b</sup> School of Materials Science and Engineering, University of Ulsan, Ulsan 44610, South Korea<sup>c</sup> Division of Materials Science and Engineering, Hanyang University, Seoul, 04763, South Korea<sup>d</sup> National Institute for Materials Science, 1-2-1 Sengen, Tsukuba, Ibaraki 305-0047, Japan

## ARTICLE INFO

## Article history:

Received 27 January 2021

Revised 11 July 2021

Accepted 20 July 2021

Available online 20 September 2021

## Keywords:

Brittle-to-ductile transition

Nano-indentation

Molecular dynamics

Dislocation

Tungsten

## ABSTRACT

Tungsten as a material exhibits broad and increasingly important applications; however, the characterization of its ductile-to-brittle transition (BDT) is currently limited to large-scale scenarios and destructive testing. In this study, we overcome this challenge by implementing small-scale techniques to provide a comprehensive understanding of the BDT behavior of pure tungsten. In order to predict the failure mode at various temperature ranges, the practical fracture analysis diagram has been proposed to describe the resistance to shear flow and cracking behavior with temperature. High temperature nano-indentation tests have provided the inherent mechanical responses corresponding to the maximum shear stress at various temperatures, which is required for dislocation activities in an atomic scaled activation volume. On one hand, atomistic simulations have provided the temperature dependence of brittle fracture stress, where the atomic bonds break due to intergranular or intragranular fracture. We considered four tungsten specimens having various microstructures prepared using different processing conditions of cold-rolling and post-annealing, and their BDT ranges were inferred using the obtained fracture analysis diagram with the statistical data processing. The fracture analysis diagram of each specimen obtained were compared with the direct observation of fracture responses in macroscopic mechanical tests, which conclusively indicated that the small-scale inherent mechanical properties are greatly relevant to the macroscopic BDT behavior in pure tungsten. Based on the BDT estimations by small-scale characterization, we provided further insights into the factors affecting the BDT behavior of tungsten, focusing on the contributions of different types of dislocations.

© 2021 Published by Elsevier Ltd on behalf of Chinese Society for Metals.

## 1. Introduction

Tungsten (W) has emerged as a promising material for use in a variety of high-temperature applications due to its unique combination of high melting point, high thermal stress resistance, and high thermal conductivity. Despite these advantages, W and its alloys are currently not being widely used as structural materials because they suffer from brittle fracture characterized by a pronounced brittle-to-ductile (BDT) behavior, even when they are in above room temperature (RT). Over the past few decades, re-

searchers have developed various methods to address the challenge of embrittlement of W and its alloys [1–7].

Among the several methods proposed to address brittle fracture in W, thermomechanical processing has been discovered to be the most effective method to improve plasticity and decrease the BDT temperature (BDTT) of W [1]. Wei et al. [3,4] suggested that thermomechanical processing effectively improved the ductility of W because it caused a redistribution of impurities through grain refinement. Reiser et al. [5] have reported that cold-rolling at temperatures below the recrystallization temperature improved cleavage resistance, resulting in a reduction in the BDTT of W from over 650 °C to below 200 °C. They proposed that an increased amount of available dislocation sources, such as low-angle grain boundaries, contributed to the change in cleavage resistance and the reduction in the BDTT. In our recent study [6], the mechanical properties of cold-rolled, hot-rolled, and recrystallized W spec-

\* Corresponding author.

\*\* Co-corresponding author.

E-mail addresses: [OHMURA.Takahito@nims.go.jp](mailto:OHMURA.Takahito@nims.go.jp) (T. Ohmura), [hnhan@snu.ac.kr](mailto:hnhan@snu.ac.kr) (H.N. Han).

imens were compared at RT. We found that the cold-rolled specimens only exhibited a plastic flow at RT while the hot-rolled and recrystallized specimens readily failed in the elastic regime. We also performed cooperative experimental and theoretical analyses based on the nano-indentation and molecular dynamic (MD) simulation to compare the stress required for the onset of plastic yielding and that required for the grain boundary (GB) fracture at RT. These investigations revealed that the remarkable plasticity of the cold-rolled specimen at RT was attributed to a high density of pre-existing mobile dislocations, indicating that the stress required for the plastic yielding is relatively lower than that required for GB fracture [6]. We realized that such a fundamental approach, e.g. the small-scale investigation on intrinsic mechanical properties, is so relevant to the macro-scale mechanical behavior of pure W. By extending the previous studies, in this study, we try to establish the sufficient knowledge on the inherent properties of W at various temperatures to comprehend its noticeable BDT behavior.

Toughness or BDTT have been standard measures to represent the mechanical properties of W materials, which has been of paramount importance to its structural integrity assessment. The BDTT is conventionally evaluated by breaking a notched bar in a pendulum-type impact tester and measuring the energy absorbed in the fracture [8,9]. However, this classic method complicates the assessment of the material where the evaluation region is limited to near the surface at the micro/nano-scale level. Currently, tungsten (W) is considered as a promising prospect for broad and increasingly important applications as plasma-facing materials in nuclear fusion reactors, as well as an apparatus for plasma-immersion ion implantation [10–12]. In these applications, the irradiation-induced damaged layer is confined to only tens of  $\mu\text{m}$ , necessitating to downsize the length scale of test specimens to examine the BDT behavior [13–16]. The BDT measurements also remain encumbered by the limitation of being a destructive methodology with notch preparation. The typical ways to fabricate a reproducible sharp notch, such as cyclic fatigue or electrical discharge machining [17], are often inappropriate for extremely hard metals like W owing to their demanding control; it requires high stress for initiating a crack and the very low stress for driving a sharp crack [18]. The introduced notch that are not sharp enough would lead to the non-conservative and unreliable results [19]. Moreover, it has been reported that the measured fracture toughness is substantially dependent on the radius of notch root that can vary depending on the way of notch preparation [17,20].

In response to these issues, we herein utilize the small-scale characterization with non-destructive testing to predict the macroscopic failure responses so that the BDT behaviors of pure W were investigated depending on the initial microstructure. The present approach is based on constructing a practical fracture analysis diagram that reflects the competition between the temperature-dependent local effective yield and fracture stresses. We performed nano-indentation tests and atomistic simulations to obtain the two competing factors, considering various temperatures and microstructural features in polycrystalline W materials. Based on the small-scale investigations, we eventually provide further insights into the contribution of different types of dislocations on plasticity of pure W.

## 2. Concept of fracture analysis diagram for pure W

The metallurgical mechanisms of BDTs have been explained using the fracture analysis diagram [8], referred to as the Yoffee diagram for structural steels [21,22], which describes a relative probability of appreciable plasticity or brittle fracture. Yoffee diagram is usually constructed based on the results of pre-processed macroscopic destructive tests and thus provides how the two stress values, effective yield and brittle fracture stresses, respectively change

with temperature. However, despite its concise and unambiguous definition, the diagram has been predominantly used for conceptual explanations rather than practical BDTT prediction. This has been attributed to the veritable difficulty in experimentally parametrizing the Yoffee diagram because the two competing factors in the diagram are usually coexist and cannot be easily distinguished in a large volume of general global deformation.

As the applied stress is increased toward the fracture, the stress in the infinitesimal volume element increases and then reaches the lattice instability limits, which are associated with inherent shear strength or tensile (cohesive) strength. At this moment, dislocation activities (nucleation or movement) or cracking behaviors (initiation or propagation) begin within the small activation volume, which eventually leads to a macroscopic failure in either a ductile or brittle manner [23,24]. Thus, it can facilitate the identification of macroscopic aspects of BDT behavior to understand the thermally activated characteristics of the intrinsic mechanical properties related to the shear and fracture strength [25,26]. Here, based on the basic concept of the Yoffee diagram, we propose another new fracture analysis diagram concept, which is more practical for the BDT estimation of pure W. The present diagram consists of local effective yield stress required for dislocation activities and local effective fracture stress for crack behavior, evaluated in terms of infinitesimal volume element in polycrystalline materials. [Fig. 1(a)]. The former represents the resistance to the onset of local plastic yielding, which can be triggered by the dislocation nucleation or movement occurring in an atomic scaled activation volume. The latter indicates the resistance to the atomic bond breaking due to intergranular or intragranular fracture. This diagram can give an indication of which one happens first, shear slip or tensile separation, in the specific volume element adjacent to the highly stressed zone, pre-cracks or flaw. If the stress necessary to permanently separate the atoms is lower than the local shear stress overall, the materials eventually undergo brittle fracture with very little micro deformation, and vice versa.

We implemented different techniques to obtain the independent characteristics of temperature-dependent local effective yield stress and fracture stress, respectively. Several researchers have suggested that the shear process of W should be modeled with dislocation plasticity, which suggests that the crack tip can be blunted and blocked by dislocation nucleation and movement, thereby suppressing crack propagation [5,7,27]. Nano-indentation is highly advantageous toward understanding the fundamental aspects of plasticity at the local volume, avoiding crack initiation that is hardly ever separated in usual macroscopic experiments [28–35]. During nano-indentation, the deformation of the surface is purely elastic at the initial loading stage. With increasing indentation load, the pressure generated beneath the indenter rises, until it surpasses the critical strength required for the onset of plasticity. These elastoplastic transition behaviors, so-called “pop-in” phenomena, are identified by the bursting of displacement under a constant load condition in a load–displacement ( $P$ – $h$ ) curve, whose activation volume has been known as several atomic volumes in bcc material [36]. The source of such pop-ins has been considered to be the nucleation of dislocations, activation of dislocation sources, or movement of pre-existing dislocations, which are well known as thermally activated processes [30–35, 37]. Therefore, we defined the first constituent part of the fracture analysis diagram, local effective yield stress, by statistically analyzing the thermally activated process of a pop-in event during nano-indentation. This also enables us to reproduce the microstructure dependence of local plastic yielding, considering the probabilistic nature of the real microstructure in several polycrystalline W materials.

Thereafter, we should acquire the necessary information on the fracture behavior of W to complete the rest of the fracture analysis diagram. The stresses required for the intergranular and in-

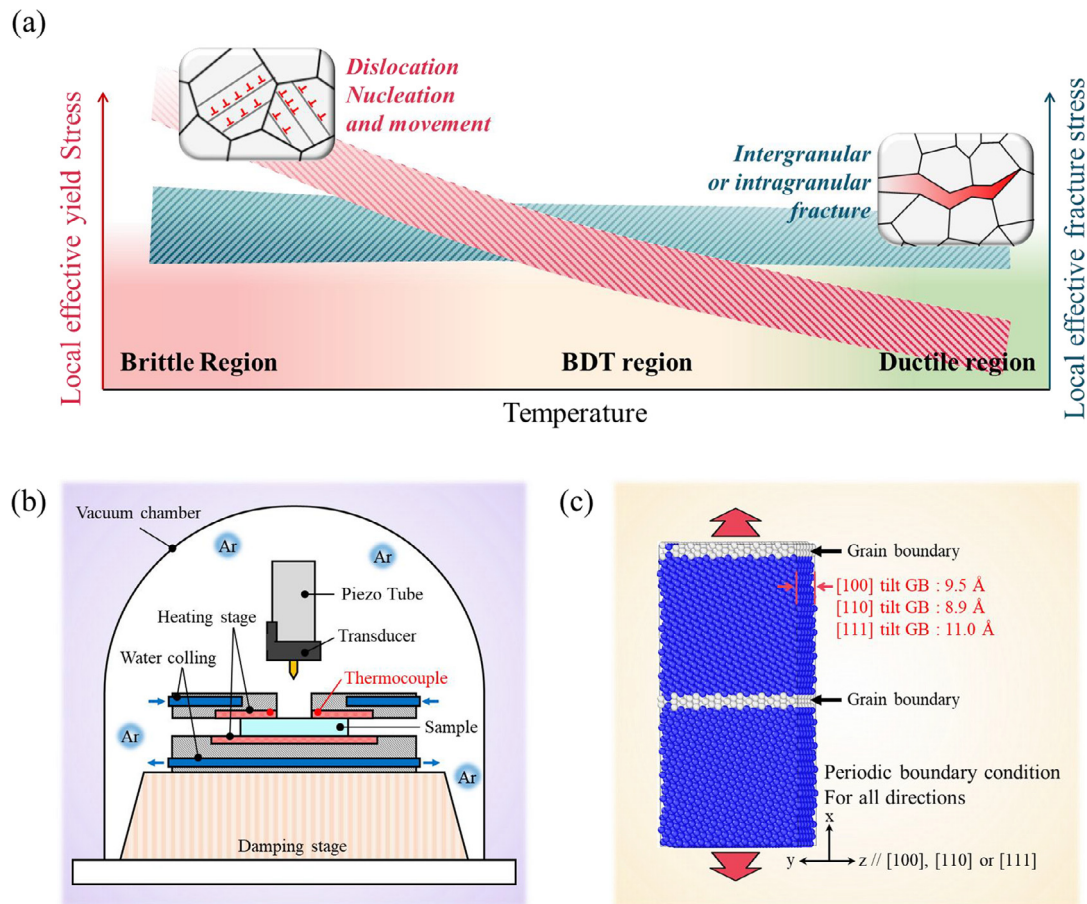


**Fig. 1.** (a) Schematic representation of the fracture analysis diagram reflecting the temperature dependence of the local effective yield and fracture stresses of the material. The intermediate temperature region represents the BDT region, where the fracture behavior of the material changes from brittle to ductile. (b) Schematic representation of a high-temperature nano-indentation system for evaluating local effective yield stress in the diagram. (c) Schematic illustration of a bcc bi-crystal cell with symmetric tilt GBs prepared for the present MD simulations. The color of atoms in the atomic snapshots is scaled according to the CNA pattern [61], where blue atoms correspond to a bcc structure and gray atoms indicate an unspecified structure.

trgranular fractures are essential facets of information to construct the diagram as the relatively weak adhesion of GBs and typical cleavage planes act detrimentally to the embrittlement of W. Because such information, excluding the effects of plastic deformation, is not readily accessible by experimental techniques, we considered simulation approaches. Density-functional theory (DFT) calculations, which can provide the most accurate projections of the intrinsic properties of GBs [38,39], cannot be singly used to provide sufficient information necessary for the fracture analysis diagram because of the high computational cost required to consider various temperatures and crack paths. Therefore, we selected an atomistic simulation that combined DFT calculations and classical molecular dynamics (MD) simulations. This method yielded a reliable interatomic potential, which was further used in the MD simulation to provide the properties of various cleavage planes and GBs at various finite temperatures.

To apply the present diagram to polycrystalline W, we should consider various grains and crack paths with individual crystallographic orientations that can stochastically govern the BDT behaviors [40,41]. Therefore, nano-indentation and atomistic simulations will provide scattered values of local effective yield and fracture stress, respectively, at a given temperature, and not just a single value. By processing these scattered stress values with a statistical approach, the fracture analysis diagram developed here provides a reasonable estimation of the specific fracture behavior at a given temperature range, as shown in Fig. 1(a).

### 3. Materials and methods

#### 3.1. Experimental procedures

In this study, we prepared four types of pure W (99.99 wt.% purity) specimens, i.e., as-received (hot-rolled), annealed, and two cold-rolled specimens having different microstructures using different processing conditions. The as-received W was fabricated via standard powder metallurgy (Plansee Group, Breitenwang, Austria), which consists of sintering above 2000 °C followed by hot-rolling and post-annealing processes. The annealed specimen was prepared by applying an additional heat treatment to the as-received specimen for 1 h at 1450 °C under a 5% H<sub>2</sub> and 95% Ar atmosphere. The cold-rolled specimens were prepared by applying an additional cold-rolling process to the as-received specimens with two different degrees of thickness reduction. The initial plate was preheated at 800 °C and rolled with iterative steps to the final reduction degree of 50% or 80%. These two cold-rolled specimens will hereafter be referred to as 50rolled and 80rolled.

We then observed the microstructure of the samples using a field emission scanning electron microscope (SEM; FE-SEM, SU70, Hitachi) equipped with an electron backscatter diffraction (EBSD) system (EDAX/TSL, Hikari). We visualized the obtained orientation information by mapping along the normal direction (ND), rolling direction (RD), and transverse direction (TD) of each specimen. To determine the dislocation density, we utilized XRD (D8 ad-

vance, Bruker) with a Cu  $K\alpha 1$  radiation source with a scan speed of  $2^\circ/\text{min}$  at RT. We used the modified Williamson-Hall (MWH) method to identify dislocation components in the specimen based on the full width at half maximum (FWHM) values of the diffraction peaks [42]. Then, the total dislocation density was calculated by applying the Convolutional multiple whole profile (CMWP) fitting procedure based on the Wilkens model [43,44]. Details for determining the fraction of edge/screw component and the CMWP analysis are provided in an online supplementary.

Nano-indentation measurements were performed using a high-temperature nano-indentation system (Hysitron, Bruker Co), housed within a high vacuum chamber on a vibration isolation stage (Minus K Technology Inc., USA) [Fig. 1(b)]. The vacuum chamber was cyclically evacuated up to a pressure of  $\sim 10^{-5}$  Torr and backfilled with Ar gas with continuous argon purging at a flow rate of 1 L/min. To minimize the occurrence of a possible thermal gradient in the sample, we used a dual heating system to heat the bottom and the top of the specimen simultaneously. Prior to the measurements, we ensured a thermal equilibrium between the probe and sample by passively heating the indenter tip for 1 h at the desired temperature. The reliability of this nano-indentation system has already been demonstrated by a previous study [45] with highly reproducible results. We performed load-controlled indentations using a diamond Berkovich tip along the ND of the W specimens with a maximum load of 2000  $\mu\text{N}$ . After measurements, we observed the indented regions using scanning probe microscopy (SPM) and EBSD to identify and exclude the results that were associated with inappropriate locations, e.g., locations that crossed GBs or scratches on the surface.

We performed instrumental tensile tests and three-point bending tests at elevated temperatures using a universal testing machine (INSTRON 5584, Instron Inc.). The tensile testing and bending system containing the specimen were placed inside a furnace and heated with a protective argon gas flow. Thermocouples were directly brought into contact with the tensile/bending specimens to monitor the exact temperature of the specimen. Miniature tensile specimens with a gauge length of 5 mm, gauge width of 1.2 mm, and thickness of 2 mm were extracted from the rolled plate in various directions. The miniature specimens for three point bending tests were manufactured in matchstick shape with the dimension of 3 mm (TD)  $\times$  2 mm (ND)  $\times$  18 mm (RD). The strain rate of the uniaxial tensile test and maximum tension part during the bending were  $10^{-3} \text{ s}^{-1}$ . Using the applied load ( $F_b$ ) and measured deflection ( $D_b$ ), the flexural stress ( $\sigma_f$ ) and strain ( $\varepsilon_f$ ) were calculated by  $\sigma_f = 3F_b L_b / 2b_b d_b^2$  and  $\varepsilon_f = 6D_b d_b / L_b^2$ , in which  $d_b$  is the thickness of the specimen,  $b_b$  is the width of the specimen, and  $L_b$  is the supporting span of the test stage ( $L_b = 10 \text{ mm}$ ).

### 3.2. Computational details

We used MD simulations to investigate the influence of temperature on the fracture stress in bcc W with differing cleavage and intergranular fractures. This information cannot be readily obtained by experiments because the fracture stress obtained by usual experiments inevitably contain effects by the dislocation activity. The present MD simulations were performed to provide this information supplementing experiments. For this purpose, all simulation cells for single-crystals and bi-crystals were prepared with the smallest lateral dimensions perpendicular to the tensile direction to minimize the occurrence of the plastic deformation during the loading.

The present MD simulations were performed using a newly developed interatomic potential for pure W based on the second nearest-neighbor modified embedded atom method (2NN MEAM) formalism [46,47]. A 2NN MEAM potential for pure W was originally developed by Lee et al. [46] with a goal of accurately repro-

ducing fundamental physical properties such as structural, elastic, and defect properties. However, this potential reproduces properties at finite temperatures, such as the melting temperature, with less accuracy. Therefore, we first developed a new potential for the pure W system and then conducted the MD simulations using the developed potential. The details on the fitting procedure of potential parameters and comprehensive benchmarks are provided in the online supplementary material.

For the development of the interatomic potential, a fitting database was constructed by performing density-functional theory (DFT) calculations for selected atomic configurations. The DFT calculations were conducted using the Vienna ab initio Simulation Package (VASP) [48–50] and projector augmented wave (PAW) method [51] within the Perdew–Burke–Ernzerhof generalized-gradient approximation (GGA) [52] for the exchange–correlation functional. In the PAW potential for W, we treated the semi core  $p$  states as a part of the valence. We used a cutoff energy of 450 eV for the plane-wave basis set and Methfessel–Paxton smearing method with a width of 0.1 eV. The Brillouin zone was sampled by the Monkhorst–Pack scheme [53] with a  $k$ -point mesh of  $21 \times 21 \times 21$  for the body-centered cubic (bcc) and face-centered cubic (fcc) primitive unit cells. The corresponding similar  $k$ -point density was employed for other structures and supercells.

We obtained the equilibrium volume ( $V_0$ ) and bulk modulus ( $B$ ) by applying the volume changes of a supercell range from  $0.95V_0$  to  $1.05V_0$  and fitted the calculated total energies as a function of volumes to the Birch–Murnaghan equation of state [54,55]. Elastic constants were obtained by applying particular strains ranging from  $-3\%$  to  $+3\%$  to an obtained equilibrium supercell. The calculated total energies as a function of strains were fitted to third-order polynomials to calculate corresponding elastic constants. Defect properties were obtained by relaxing atomic positions at a constant volume and cell shape, with the convergence criteria for energy and forces set to  $10^{-6}$  eV and  $10^{-2}$  eV/Å, respectively. The vacancy migration energy with a suitable saddle-point configuration was calculated using the nudged elastic band (NEB) method [56,57]. The surface energy was calculated using rectangular cells with a stacking of 11 Å to 13 Å thick slabs and a vacuum region of 10 Å. We performed phonon calculations using the “Phonopy” code [58,59] with a bcc supercell of 128 atoms. In the phonon calculation, the convergence criteria for energy and forces were set to  $10^{-8}$  eV and  $10^{-4}$  eV/Å, respectively. For the atomic configurations at finite temperatures, we performed two-step DFT calculations according to the concept of the UP-TILD method [60]. First, ab initio MD simulations were performed based on relatively low DFT convergence parameters for a total of 1000 steps with a timestep of 1.5 fs. To determine accurate energies and forces of each configuration at finite temperatures, we also performed subsequent well-converged calculations with a higher cutoff energy and denser  $k$ -point mesh using obtained snapshots from ab initio MD simulations.

We further used the DFT calculations to verify the performance of the developed 2NN MEAM potential in reproducing the ideal tensile stress of bulk bcc W. To avoid undesired interactions between periodic images, we initially prepared all cells for DFT calculations with a vacuum region of 20 Å along the ND of the designated fracture surface. We then calculated the ideal tensile stress based on the separation energy versus separation distance response of bcc W. The response was calculated by separating pre-divided regions of a simulation cell without atomic relaxation. The corresponding tensile stress  $\sigma$  was calculated according to the following equation:

$$\sigma_t = \frac{1}{\Omega(\varepsilon)} \frac{\partial E_t}{\partial \varepsilon} \quad (1)$$

where  $E_t$  is the total energy and  $\Omega(\varepsilon)$  is the volume at the given tensile strain  $\varepsilon_t$ .

MD simulations were then performed to examine the intragranular and intergranular fracture stresses of bcc W based on the developed 2NN MEAM potential. We first prepared single-crystal cells with loading directions of [100], [110], and [111] to examine the intragranular fractures. The dimension of the single-crystal cells along the loading direction was set to be larger than 45 Å. For the GB fracture, [100], [110], and [111] symmetrical tilt GBs with diverse misorientation angles were selected as representative GBs, which included the special, low-angle, and high-angle GBs. Each GB was prepared as a part of the bi-crystal cell with periodic boundary conditions along all three dimensions [Fig. 1(c)]. The dimension of bi-crystal cells along the loading direction was selected to be larger than 90 Å. Initially, equilibrium GB structures were prepared by an energy minimization process at 0 K with the rigid-body translation of one grain relative to another. We then selected the most stable configuration for further loading. Atomic arrangements were identified using a common neighbor analysis (CNA) algorithm [61], as implemented in the open visualization tool (OVITO) program [62].

All MD simulations were carried out using Large-scale Atomic/Molecular Massively Parallel Simulator code [63], employing a time-step of 2 fs. We controlled temperature and pressure with a Nosé–Hoover thermostat and barostat [64,65], respectively. Initially, the simulation cells generated were relaxed by performing MD runs in an isobaric–isothermal (NPT) ensemble at the designated temperature and zero pressure. We then applied a strain-controlled tensile loading by changing the cell dimension along the loading direction. A strain rate of  $5 \times 10^8 \text{ s}^{-1}$  was selected considering our previously published benchmark simulations that examined the effect of strain rates on the general GB fracture stress [6]. During the tensile loading, we fixed the dimensions in the directions that were perpendicular to the tensile direction to induce a triaxial stress state near the GB, similar to the experimental condition, and to encourage GB fracture.

## 4. Results

### 4.1. Microstructural evolution and dislocation density

The crystallographic orientations of each specimen are presented in Fig. 2(a), using colored cuboidal surface maps. The cold-rolled (80rolled and 50rolled) specimens were characterized by a pancake-like structure with extremely flattened and elongated grains that were subdivided by the deformation-induced low-angle GBs. The average grain size of each specimen was determined according to the line intercept method using GB maps along the RD and TD. The representative EBSD GB maps, used to identify the individual grain, and resultant distribution of grain sizes of each specimen are illustrated in the supplementary material provided (Fig. S4). The average grain sizes of 80rolled and 50rolled specimens were 1.36  $\mu\text{m}$  and 6.90  $\mu\text{m}$ , respectively. The as-received specimen also had a slightly deformed structure, as identified by the presence of low misorientation angles inside the individual grains. However, the average grain size (31.15  $\mu\text{m}$ ) was much larger than that of the cold-rolled specimens. After annealing at 1450 °C, the deformed grains were recrystallized and grown, thereby resulting in equiaxed morphologies with a grain size (76.56  $\mu\text{m}$ ) that was much larger than those of the other specimens.

The dislocation densities distinguishing the edge and screw components were determined based on the FWHM values according to the MWH method [Fig. 2(b)]. Because the theoretical  $q$  values for the pure edge (−0.841) and screw (2.034) dislocations reported by Ungár et al. [66] correspond to ideal cases, the experimentally obtained  $q$  values for the combination of screw and

edge dislocations should be present between the theoretical values. The relative ratio of the edge component was calculated by comparing the experimental measurements with the theoretical values. For the as-received specimen, the proportions of the edge (56%) and screw (44%) components were comparable, but the cold-rolling and annealing treatments caused changes in the proportion of each dislocation component in the opposite direction [Fig. 2(c)]. The proportion of the edge component was maximized in the most severely deformed specimen (80rolled). The CMWP fitting was then used to determine the dislocation density of each specimen type. We observed large differences among the dislocation densities, which was consistent with the results of the microstructure analysis. The cold-rolled specimens exhibited high total dislocation densities (80rolled:  $3.43 \times 10^{15} \text{ m}^{-2}$ ; 50rolled:  $1.30 \times 10^{15} \text{ m}^{-2}$ ), which corresponded to the typical values obtained from heavily cold-rolled materials [67]. The as-received specimens also contained a considerable amount of dislocations, but their density was substantially lower than that of the cold-rolled specimens (as-received:  $3.51 \times 10^{14} \text{ m}^{-2}$ ). This was because the as-received specimens underwent a hot-rolling process above the recrystallization temperature and subsequent post-annealing process to reduce the internal residual stress. After annealing at 1450 °C, the specimen was recovered and fully recrystallized with a dislocation density of  $3.78 \times 10^{12} \text{ m}^{-2}$ .

### 4.2. High-temperature nano-indentation

We characterized the intrinsic mechanical properties related to the local plastic yielding of W at elevated temperatures using nano-indentation tests. The resultant  $P$ – $h$  curves of the as-received specimen are presented as examples in Fig. 3(a). The dashed lines in Fig. 3(a), which coincide with the initial stage of the  $P$ – $h$  curves, are the theoretical Hertzian elastic contact solutions for a spherical indenter [68], expressed as:

$$P = \frac{4}{3} E_r \sqrt{Rh^3} \quad (2)$$

where  $P$  and  $h$  denote the load applied by a spherical indenter tip and the corresponding indentation depth, respectively;  $E_r$  is the reduced elastic modulus considering the elastic displacements of both the indenter and the sample, which is determined at the initial unloading portion of each indentation curve [28]; and  $R$  is the effective radius of the indenter tip. The  $P$ – $h$  curves for all the specimen types exhibit sudden jumps in the displacement that deviated from the Hertzian elastic solution, which are referred to as pop-ins. The maximum shear stress ( $\tau_{max}$ ) associated with the onset of plastic yielding can be calculated as [68]:

$$\tau_{max} = \frac{0.47}{\pi} \left( \frac{4E_r}{3R} \right)^{2/3} P_p^{1/3} \quad (3)$$

Here,  $P_p$  is the load at the pop-in event and  $R$  can be obtained by fitting the elastic region of all the indentation curves with Eq. (2). The cumulative probabilities of the experimental  $\tau_{max}$  values for the as-received specimen at various temperatures are shown in Fig. 3(b). The obtained probabilities of  $\tau_{max}$  can be fitted using a lognormal distribution function, which is usually applied to the probabilistic design of engineering phenomena with a large statistical variance and all-positive values [69]. Fitting examples for the as-received specimen at different temperatures are shown by the solid lines in Fig. 3(b). Similar processes have been applied to other specimens (80/50rolled and annealed), and the results are shown in supplementary Fig. S5.

The typical  $P$ – $h$  curves of each specimen at different temperatures in Fig. 3(c) correspond to the experimental results with a cumulative probability close to 0.5 at a given temperature. Below the  $P$ – $h$  curves for each specimen, indentation curves are dis-

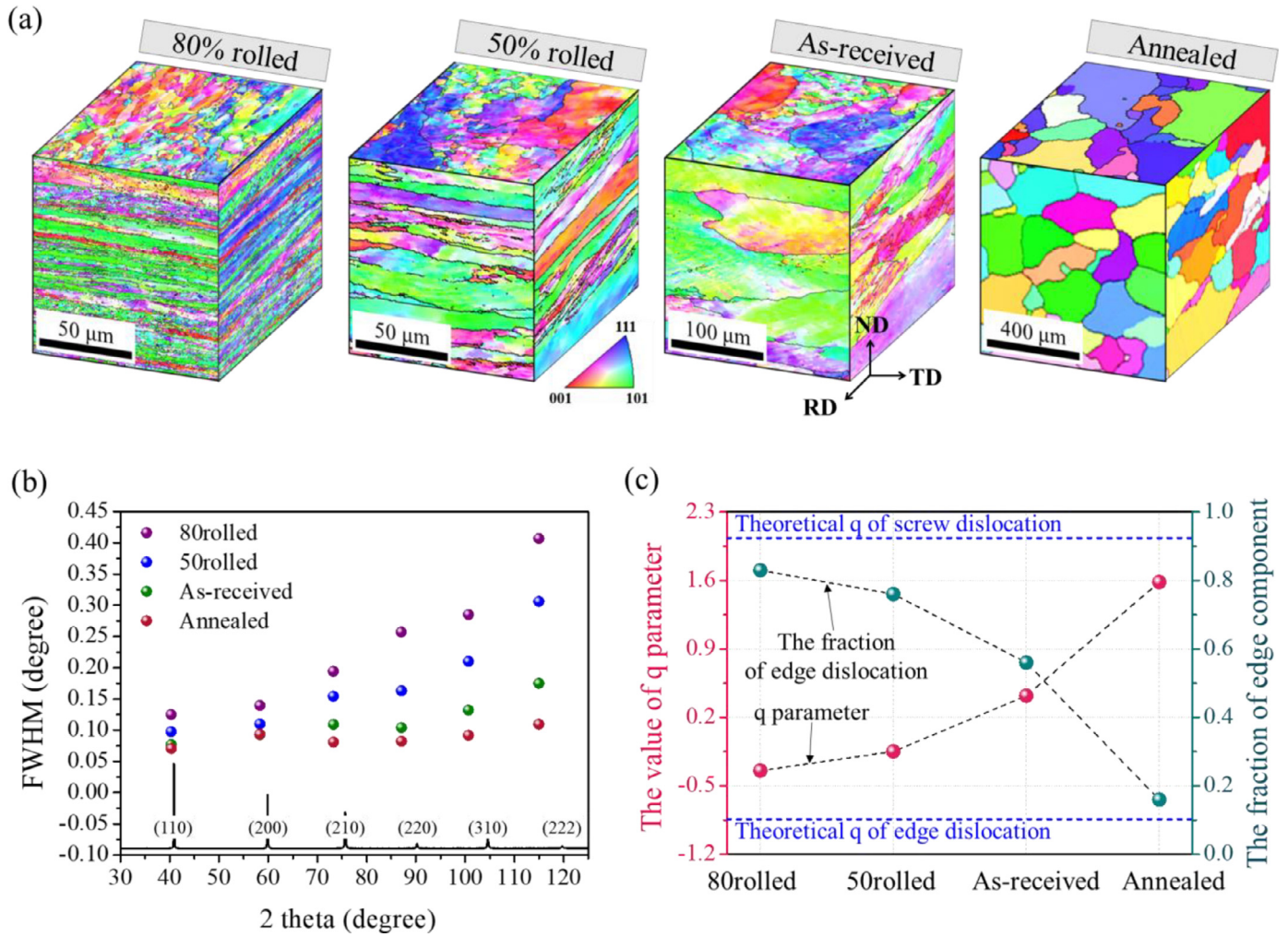


**Fig. 2.** (a) EBSD orientation maps of 80rolled, 50rolled, as-received, and annealed specimens. To clarify the grain shape of each specimen, their crystallographic orientations of each specimen are presented using colored cuboidal surface maps along the ND, RD, and TD. (b) FWHM values obtained at major diffraction peaks of bcc W using CuKα1 radiation. (c) Experimental  $q$  values and the fraction of edge component calculated using the MWH method. Red dotted lines correspond to the theoretical  $q$  values for the pure screw (2.034) and pure edge (−0.841) components [42].

placed along the x-axis, only showing the loading portions in clarity. This obviously shows that the pop-in stress at RT decreases as the degree of deformation increases. The average values of corresponding  $\tau_{max}$  are  $9.70 \pm 1.79$  GPa for 80rolled,  $11.09 \pm 1.98$  GPa for 50rolled,  $12.84 \pm 3.14$  GPa for as-received, and  $17.27 \pm 2.62$  GPa for annealed specimen; these are between Peierls-Nabarro stress for {211}<111> slip system of W (~7.28 GPa) and theoretical shear strength of W ( $\tau_{th} \sim 25$  GPa) [6,70]. If the W specimen contains large amount of dislocations, it is very plausible that indenter tip contacts the pre-existing dislocations during nano-indentation. Otherwise, in the annealed specimen, the indenter mainly encounters the dislocation free zone, primarily resulting in a nucleation of dislocation. Thus, reduction of  $\tau_{max}$  in highly deformed W is attributable to the lower stress required for activation of pre-existing dislocations compared to dislocation nucleation in the dislocation free zone [6]. This further implies that plasticity of W specimens in our study is influenced by multiple factors such as heterogeneous dislocation nucleation, dislocation source activation and movement of pre-existing dislocations, while their contributions to the onset of plastic yielding are different between each specimen.

We found that the characteristics of the plastic deformation depended, to a large extent, on temperature [Fig. 3(c)]. When the tests were performed at higher temperatures, the maximum indentation depth increased and the pop-in load decreased. Note that

the pop-in behaviors are controlled by the nucleation and glide of dislocations, which are thermally activated kinetic processes. According to the concept proposed by Mason and Schuh et al. [31,35], the local rate where the pop-ins occur ( $\dot{n}$ ) can be expressed using an Arrhenius-type equation:

$$\dot{n} = \frac{dn}{dt} = \eta \exp\left(-\frac{Q - \tau_{max}V^*}{kT}\right) \quad (4)$$

Here,  $\eta$  is the pre-exponential factor,  $Q$  is the activation enthalpy, and  $V^*$  is the activation volume. This equation implies the first displacement burst rate for a unit volume of material under a specific stress state. In this analysis, the local rate integrated over the indented volume is  $\dot{N}$ , and the cumulative fraction function of the pop-ins against time ( $t$ ) are expressed by  $F(t) = 1 - \exp(-\int_0^t \dot{N} dt)$ . Considering the relationship between  $P$  and  $t$  ( $P = \dot{P}t$ ), and the definition of  $\tau_{max}$  [Eq. (3)],  $F(t)$  can be converted to cumulative load statistics  $[F(P)]$ .

$$F(P_p) = 1 - \exp\left\{ \frac{-\frac{9K\rho\eta}{4E_p P_p \alpha^6} \exp\left(-\frac{Q}{kT}\right) [120 + \exp(P_p^{1/3} \alpha)]}{\left. \begin{aligned} & \cdot (P_p^{5/3} \alpha^5 - 5P_p^{4/3} \alpha^4 + 20P_p \alpha^3 - 60P_p^{2/3} \alpha^2) \\ & + 120P_p^{1/3} \alpha - 120) \end{aligned} \right\}} \quad (5)$$

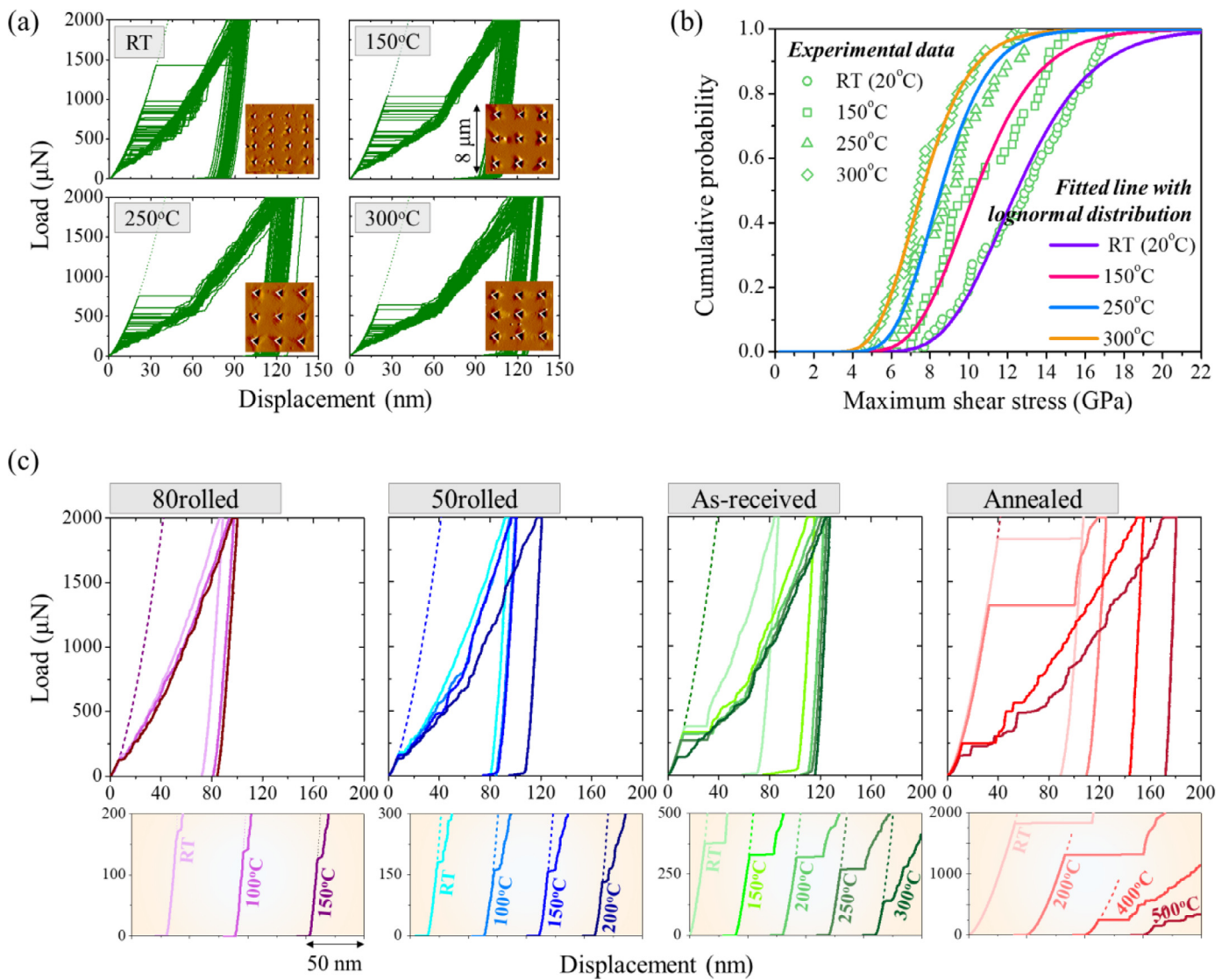


**Fig. 3.** Results of high-temperature nano-indentation tests to obtain the critical shear stress value for the onset of plastic yielding. (a)  $P$ - $h$  curves of the as-received specimen at RT and elevated temperatures. Insets are SPM images that show a part of the indented area after the unloading. (b) Cumulative probability of the  $\tau_{max}$  experimentally obtained for the as-received specimen at different temperatures. Solid lines correspond to the best fit obtained between the experimental data and cumulative distribution function of the lognormal distribution. (c) Typical  $P$ - $h$  curves of all the W specimens at RT and elevated temperatures. Among the various results obtained under certain conditions, the results with a cumulative probability of approximately 50% are shown as examples. Magnified images exhibiting the pop-in event are presented separately below each figure.

$$\alpha \equiv \frac{0.47}{\pi} \left( \frac{4E_r}{3R} \right)^{2/3} \frac{V^*}{kT} \quad (6)$$

Given the Eqs. (4)-(6), we can finally find the linear relation between the temperature and  $\tau_{max}$ :

$$\tau_{max} = \gamma'_p kT + \frac{Q}{V^*} \quad (7)$$

Here,  $\gamma'_p$  is a complex function that depends on cumulative probabilities of  $\tau_{max}$ ,  $F(\tau_{max})$ . A more detailed extension of above equations is described in supplementary material. Using Eq. (7), we can obtain the temperature dependence of  $\tau_{max}$  by linearly plotting the  $\tau_{max}$  values corresponding to the specific  $F(\tau_{max})$ , which are extracted from the statistically predicted distribution of the experimental data in Fig. S5. Upon plotting the data points at  $F(\tau_{max}) = 0.1, 0.3, 0.5, 0.7,$  and  $0.9$ , along with the corresponding linear functions, it was revealed that  $\tau_{max}$  decreased as the operating temperature increased for all specimens (Fig. 4).

#### 4.3. Fracture stress with the variation of temperature

We performed a series of MD simulations to examine the fracture stress of selected cleavage planes and GBs. We first examined the reliability of the developed interatomic potentials in reproducing properties that were closely related to the fracture behavior. First, the ideal tensile stress of the bulk single crystal for typical cleavage planes was selected as the target property and compared using the developed potential and DFT. The ideal resultant tensile stresses of bcc W for the separation of the [100], [110], and [111] planes agreed well with the maximum tensile stress calculated between the developed potential and DFT calculations [Fig. 5(a)]. Thereafter, MD tensile simulations at finite temperatures were performed in a temperature range of 50–850 K at intervals of 50 K, considering the loading directions of [100], [110], and [111]. The MD tensile simulations confirmed that the overall fracture stress was lowest in the tensile loading along the [100] direction for all temperature ranges [Fig. 5(b)]. This result was consistent with the well-known preference for the (100) cleavage of bcc W [27,71].

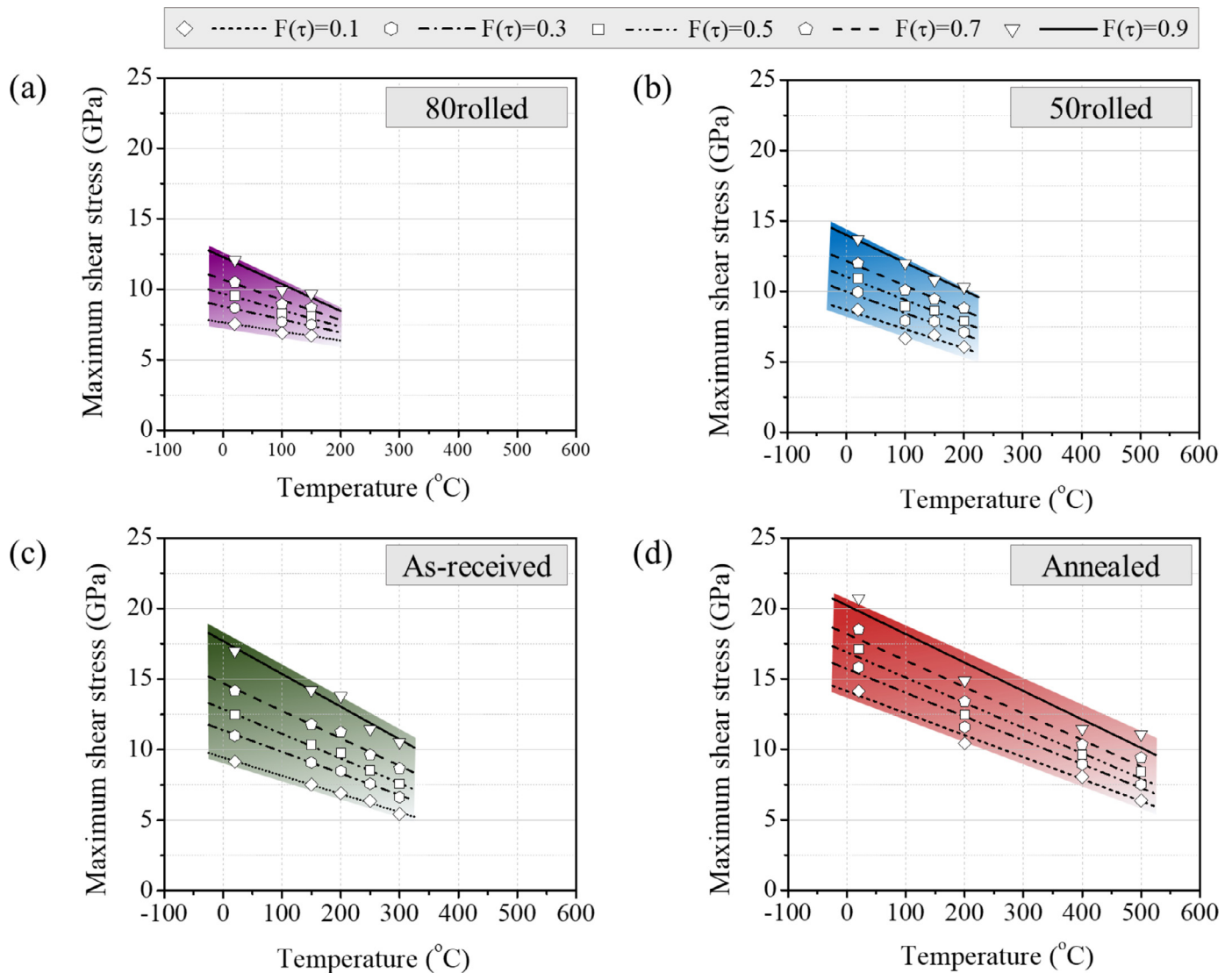


**Fig. 4.** Temperature dependence of the  $\tau_{max}$  obtained for the (a) 80rolled, (b) 50rolled, (c) as-received, and (d) annealed specimens. Experimental data at selected cumulative probabilities ( $F(\tau) = 0.1, 0.3, 0.5, 0.7,$  and  $0.9$ ) are presented along with the corresponding linear regression of data points [Eq. (7)].

The calculation of the GB fracture stress was conducted by first evaluating the performance of the developed potential in describing the GB energy, which was expected to be closely related to the fracture behavior of the GBs. We found that the energies of representative GBs that were calculated based on the developed potential were in excellent agreement with the reported DFT data [72] [Fig. 6(a)]. The MD tensile simulations were then performed with bcc bi-crystal cells in a temperature range of 50–850 K at intervals of 50 K based on the developed potential. Fig. 6(b) presents the stress-strain responses of selected bi-crystal cells with special ([100] tilt  $36.9^{\circ}$ ,  $\Sigma 5$ ), low-angle ([110] tilt  $10.1^{\circ}$ ), and high-angle ([111] tilt  $32.2^{\circ}$ ) GBs as examples. All the bi-crystal cells deformed elastically at the initial stages of tensile loading. After significant loading, fracture was observed in most of the cells without any plastic deformation. Several MD runs, especially those at very high temperatures, exhibited twinning prior to the fracture event, accompanied by an additional stress drop in the stress-strain response. We defined the GB fracture stress as the maximum tensile stress regardless of the occurrence of twinning because the stress at the fracture event was generally comparable or greater than that at the twinning event. The resultant GB fracture stress was much

less dependent on the misorientation angle, with few exceptions in the case of special GBs [Fig. 6(c)], compared to the trend of GB energies [Fig. 6(a)].

The MD simulation results revealed that the GB fracture stresses [Fig. 6(c)] were generally lower than the cleavage fracture stresses [Fig. 5(b)], even after considering the statistical variance. This result implies that the fracture along the GB controls the overall embrittlement process of W, which is consistent with the reported preference of the intergranular fracture [73]. Therefore, we used the calculated GB fracture stress to construct the fracture analysis diagram, rather than the cleavage fracture stress. To compare these measurements with the  $\tau_{max}$  measured through nano-indentation, we converted the obtained normal fracture stress to the shear state. Because the  $\tau_{max}$  is defined as half of the normal stress in a state of uniaxial tension, the critical shear stress for the fracture can be defined as half of the obtained fracture stress [8]. As shown in supplementary Fig. S6, we developed distribution patterns of the converted shear stress for GB fracture, considering all simulation results. The results were fitted using the lognormal distribution function to determine the statistical significance at each temperature.

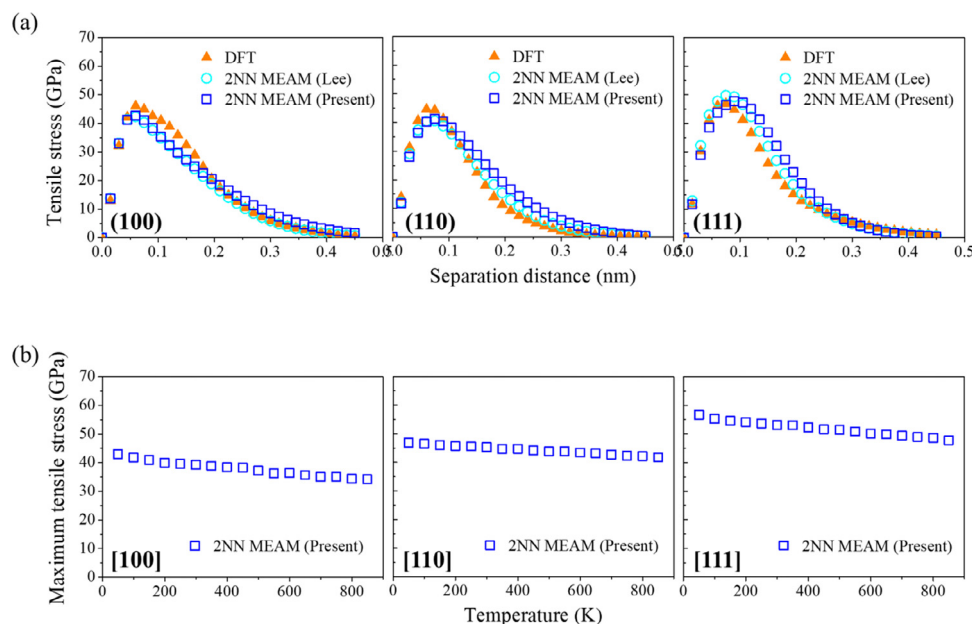


**Fig. 5.** Ideal (theoretical) mechanical responses in tensile simulation of bcc W single crystals for usual cleavage planes. (a) The resultant ideal stress–distance responses of predefined fracture surfaces of (100), (110), and (111) calculated using the molecular statics simulations based on present and previously published [46] 2NN MEAM potentials compared to the present DFT calculation. (b) Fracture stresses of bcc single crystal cells for the loading directions of [100], [110], and [111], which were obtained using MD simulations according to the present 2NN MEAM potential.

#### 4.4. Direct observation of fracture behavior during macro mechanical tests

We directly observed the failure responses at various temperatures by implementing uniaxial tensile and three-point bending tests. Comparison of stress-strain curves between the W specimens are represented in Fig. S7, and the orientation dependency of tensile response in as-received specimen is shown in Fig. S8. At RT, all specimens exhibited negligible plastic strains, thereby indicating that the BDTs of all the specimens were higher than RT. As the testing temperature increased, the flow stress decreased and the plastic strain became more visible after a certain temperature, which appeared differently in the four W specimens. To obtain a detailed insight into the BDT behavior, the fractures appearing in several selected specimens were identified after tensile tests [Fig. 7(a)]. Each value of energy absorbed exhibited in Fig. 7 was calculated by integrating the measured load-displacement (deflection) curve (Fig. S7) from the yield to fracture points, which represented the amount of energy the testing specimen accommodated during plastic deformation. The SEM images of the fractured specimens indicated that the fracture appeared to be a mixed type of cleavage and intergranular brittle fractures. According to the results of MD simulations, the fracture must have begun in intergranular manner. However, the subsequent crack deflection might follow the different paths depending on the propagation direction due to the grain shape anisotropy in rolled W specimen [74]. As the intergranular fracture is supposed to be geometrically hindered when the crack is oriented along ND, cleavage type would lead to the final failure across the specimen. This might result in both of intergranular and cleavage fracture appearances on the RD planes (Fig. S9). Nevertheless, the fracture morphologies of the tests performed at relatively lower and higher temperatures seemed sufficiently different to distinguish before and after the BDT. The former cases showed an absence of necking and apparently brittle fracture mode after a limited amount of plastic strain (Fig. S7). They absorbed non-zero energy of plastic deformation, but still appeared to be in brittle region. This implies that the present specimens cannot take on a ductile aspect by absorbing only about

450 J of plastic energy. Conversely, the fracture morphologies of the specimens tested at higher temperatures with relatively larger elongation exhibited distinct necking, which could be regarded as a sign of significant plasticity induced by the dislocation slip.

The three-point bending test also showed a similar BDT aspect between the W specimens [Fig 7(b, c)]. At 300 °C, the as-received specimen was rapidly broken into two pieces, whereas the specimen tested at 380 °C was fully ductile, exhibiting a large strain and bending angle of approximately 20% and 30°, respectively. In the intermediate temperature regime, the specimens were bent by approximately 10° (9° at 330 °C and 12° at 340 °C) and were observed to contain the bold cracks passing through the specimens. This implies that the BDT of the as-received specimen occurs between 300 and 380 °C, which is consistent with the results of the uniaxial tensile test. The same aspect was found in the other specimens exhibiting BDT behaviors in the same temperature range between tensile loading and bending (Fig. S7).

## 5. Discussion

### 5.1. Probabilistic approach to determine the BDT region in the fracture analysis diagram

In Sections 4.2 and 4.3, we examined the temperature dependences of the critical shear stress required for the onset of local plastic yielding (Fig. 4) and GB brittle fracture (Fig. 6) using the high-temperature nano-indentation and MD simulations. Since both the experimental and simulation results were obtained with various grains and GBs resulting in scattered values, we first need to designate the confidence intervals of the data sets for constructing the fracture analysis diagram. As the two standard deviations ( $2\sigma$ ) away from the mean ( $\mu$ ) value are frequently used to establish the statistic confidence intervals with the lowest cutoff value in the hypothesis test [75], the data distributions of local effective yield and fracture stresses were finally figured with the interval of  $\mu \pm 2\sigma$ . The corresponding ranges of  $\tau_{max}$  depending on temperature are represented by red shaded areas in Fig. 8, which were extracted from the cumulative probabilities of lognormal distribution

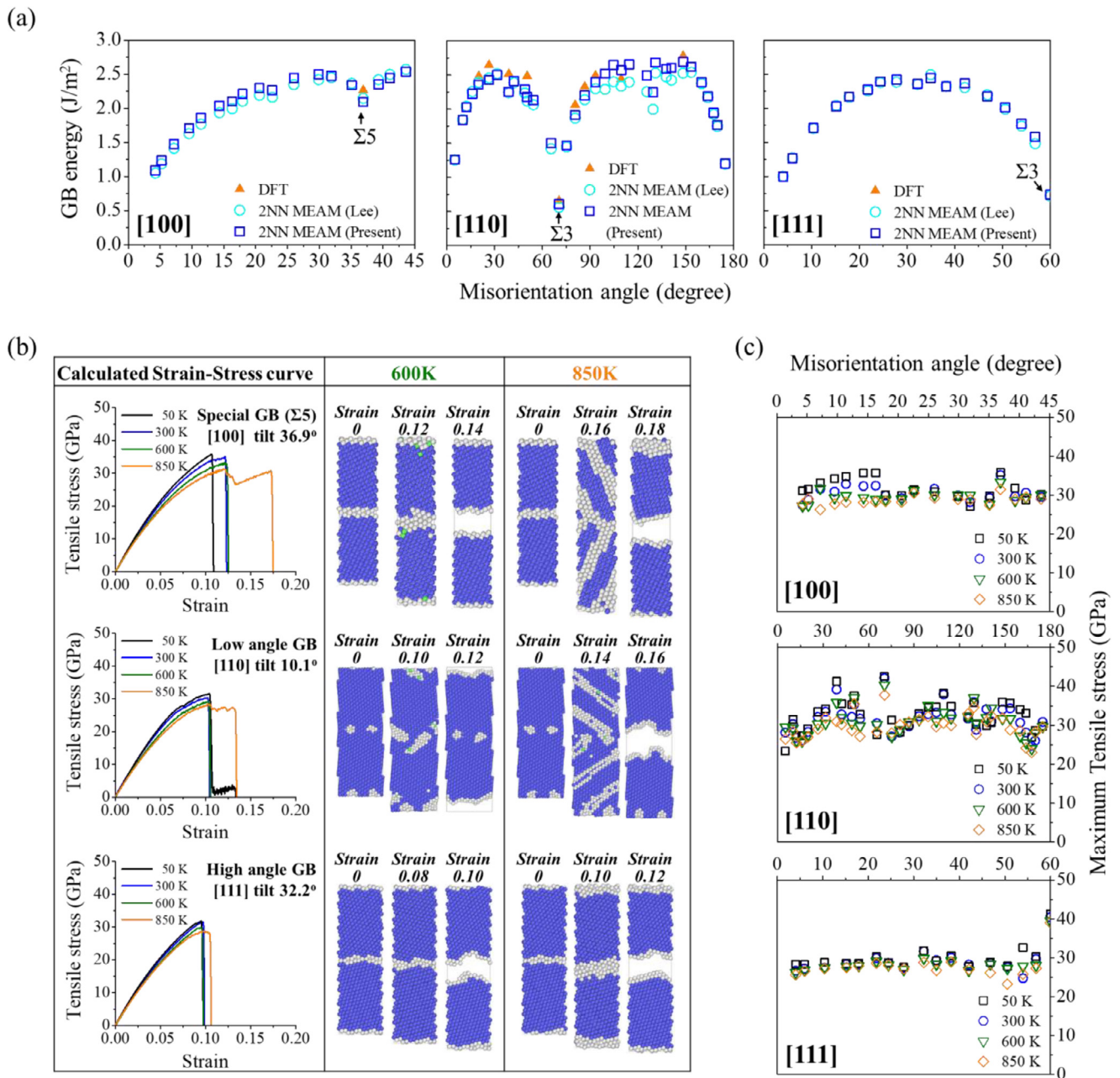


**Fig. 6.** Fracture behavior of tilt GBs with diverse misorientation angles in pure W. (a) GB energies of [100], [110], and [111] symmetrical tilt GBs in bcc W calculated using molecular statics simulations based on the present and previously published [46] 2NN MEAM potentials compared to the present DFT data [72] (b) Tensile stress-strain responses of bcc bi-crystal cells with special ([100] tilt 36.9°,  $\Sigma 5$ ), low-angle ([110] tilt 10.1°), and high-angle ([111] tilt 32.2°) GBs calculated via the MD simulations based on the 2NN MEAM potential developed in this study. Results of tensile loadings at selected temperatures (50, 300, 600, and 850 K) are presented as examples. Snapshots of bi-crystals at selected temperatures and different levels of strains are also presented. The color of atoms in the atomic snapshots is scaled according to the CNA [61] pattern. (c) Fracture stresses of symmetric tilt GBs with various misorientation angles. Results of tensile loadings at selected temperatures (50, 300, 600, and 850 K) are presented as examples.

of  $\tau_{max}$  (Fig. S5). The statistical ranges of fracture stress were also determined as the interval of  $\mu \pm 2\sigma$  in the same manner as the preceding case (Fig. S6), which are represented by the blue-shaded areas in Fig. 8.

Subsequently, the relevant boundary conditions to define the BDT regime was set based on physical meaning. Here, we considered the role of local events, which are dislocation activities or cracking, on global failure mode. Note that each  $\tau_{max}$  value obtained from the pop-in event results from the specific slip system in an atomic-level activation volume, which is favorable in terms of indentation direction and grain texture. Because the

macroscopic plastic deformation of polycrystalline materials occurs through a cooperative deformation process with satisfying the compatibility between strain components in infinitesimal volume element [8], the single pop-in event itself cannot lead to the global yielding behavior. Therefore, we should adopt the borderline of  $\tau_{max}$  in consideration of the possibility that a sufficiently large amount of local plasticity can occur to represent the ductile trend. The criteria of  $\tau_{max}$  to define the BDT region was eventually determined as the maximum limit of statistical distribution, which corresponds to  $\mu + 2\sigma$  in  $\tau_{max}$  [ $F(\tau_{max}) = 0.9772$ ], as highlighted by the red solid line in Fig. 8.

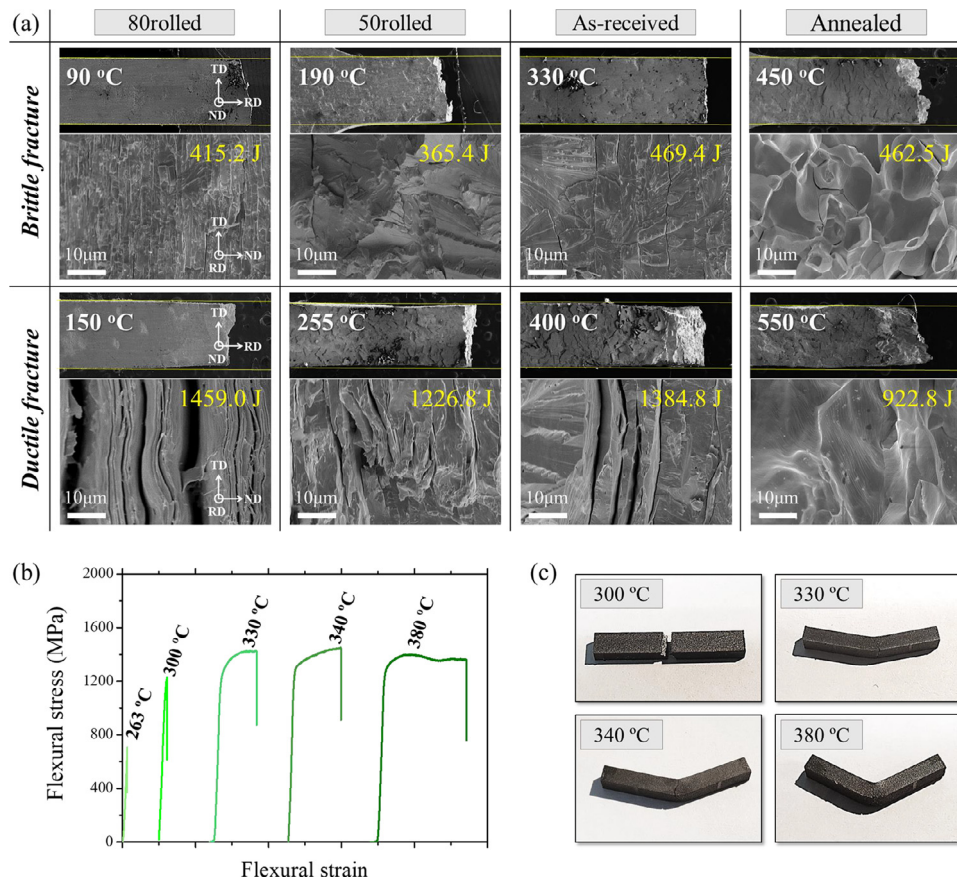


**Fig. 7.** (a) Fractographs observed by the SEM after the tensile tests at different temperatures. The upper parts show the fracture morphologies of tests performed at lower temperatures and the lower parts at relatively higher temperatures. The corresponding values of energy plastically absorbed during the tensile loading are noted in the figures with yellow color. (b) Typical flexural stress–strain curves of three-point bending tests for selected as-received specimens as an example. (c) Fractured specimens corresponding to each curve in (b), showing BDT.

In aspect of fracture in brittle materials, we need to be aware of the possible weakest-link behavior; even a small amount of crack event can dominate the resulting brittle failure, i.e., the earliest crack would be nucleated at the GB with a minimum fracture strength, which in turn quickly leads to a macroscopic brittle fracture. Taking this into account, we defined the fracture strength criteria in the present fracture analysis diagram as the minimum values in its  $\mu \pm 2\sigma$  distribution. Although it is highly unlikely that GBs belonging to less than  $\mu - 2\sigma$  exist in the material, we should consider this rare possibility as the crack initiation is more sensitive when determining whether the material behaves in a ductile or brittle manner. Once a crack is nucleated at any site, even with an extremely rare potential, a brittle fracture will certainly become dominant. Thus, we introduced one more criterion of  $\mu - 3\sigma$  for fracture strength to consider as many crack sites as possible. The two borderlines ( $\mu - 2\sigma$  and  $\mu - 3\sigma$ ) of fracture strength for the BDT regime are represented by the blue-dotted and solid lines in Fig. 8.

By determining the meaningful boundaries for the  $\tau_{max}$  and GB fracture shear stress, the fracture analysis diagram for each specimen type was completed, as shown in Fig. 8. There are two intersection points between the red and blue solid/dotted lines, dividing the present fracture analysis diagrams into three parts according to the temperature. In the first section, at a relatively lower temperature, the  $\tau_{max}$  is mostly higher than the fracture strength. In this temperature range, if the crack is nucleated at any site within the specimen, the crack can readily propagate without extensive plastic deformation. The temperature range above the upper intersect represents the ductile region wherein the local shear stress

required for plastic deformation is lower than the fracture stress, resulting in a completely ductile fracture. The intermediate temperature regime between the two intersects can be defined as the BDT region wherein the BDT can occur in a material. In this temperature region, the failure behavior is governed by experimental conditions (e.g., specimen dimension or loading direction) and stochastic factors, including thermal fluctuation, such that the plastic flow or brittle fracture occurs probabilistically and are mixed in some cases.

## 5.2. Comparison between the present fracture analysis diagram and macroscopic failure behavior

Fig. 9(a) shows the variation of absorbed energy with temperature for each specimen measured by uniaxial tensile and three-point bending tests, corresponding to the results represented in Fig. S7. The absorbed energy gradually increased with temperature, without a sharp step in the curve. Because of such an ambiguous transition behavior, the real BDTT values have been determined in a different manner depending on material type (e.g., at 50% of the fracture energy, the upper shelf in the fracture energy, or the specific energy value, such as 20 J in low-strength ship steels) or sometimes defined as a whole transition region from lower to upper shelf, and not a single value [8,76].

For comparison, the BDT regions of each specimen obtained using the present fracture analysis diagrams are also presented in Fig. 9. In Section 4.4, we inferred the boundaries of BDT regime based on the fracture surface observation (Fig. 7), which indicated that the BDT can occur above the temperature range where

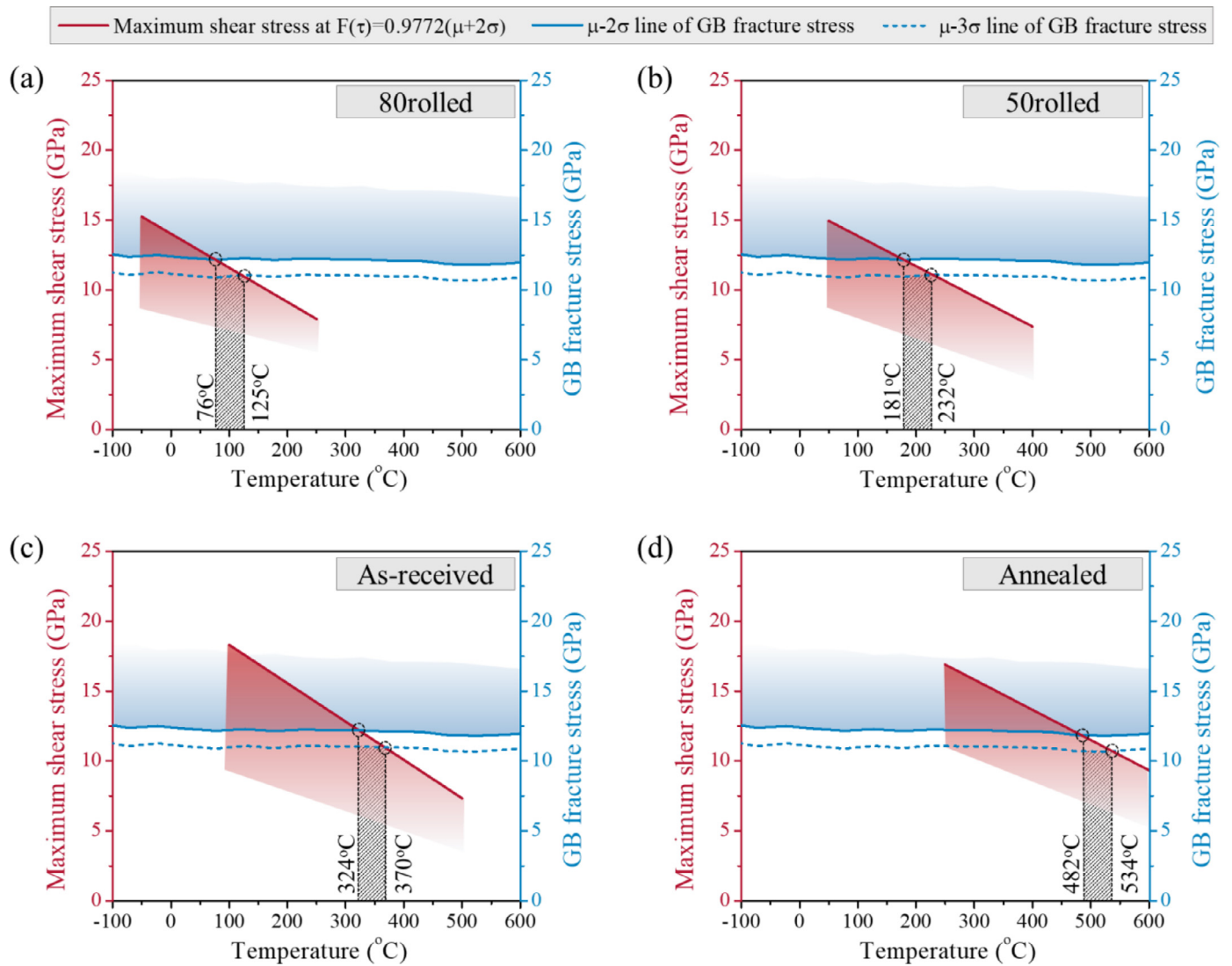


**Fig. 8.** Present fracture analysis diagram of (a) 80rolled, (b) 50rolled, (c) as-received, and (d) annealed W specimens established by combining the  $\tau_{max}$  measured using nano-indentation and fracture shear stress obtained using MD simulation. The red solid line indicates the temperature dependence of the  $\tau_{max}$  at  $[F(\tau) = 97.7\%]$  corresponding to  $(\mu+2\sigma)$ . Blue-colored solid and dotted lines correspond to the  $(\mu-2\sigma)$  and  $(\mu-3\sigma)$  of data points for the GB fracture stress, respectively. Here,  $\mu$  is the mean of the distribution and  $\sigma$  is its standard deviation determined by the lognormal distribution fitting (Fig. S5 and S6). The BDT region corresponds to the range between two intersects of red solid and blue solid/dotted lines (gray-hatched areas).

the W specimens can accommodate at least about 450 J of energy by plastic deformation. Regardless of the specimen type, the estimated BDT regions were located well within the experimental transition regions, indicating a qualitative agreement between them. Directly measured features, such as lower BDTT for the cold-rolled specimens and higher BDTT for the annealed specimens, were accurately reproduced by the method developed in this study.

Notably, the fracture behaviors of W can be influenced by the testing method and experimental conditions, such as the dimensions of the specimens, strain rate, and loading direction. For example, if the specimen is machined with a notch or stretched at a higher strain rate, the flow stress during destructive testing is raised due to plastic constraint, resulting in a slight shift of the absorbed energy versus temperature curve toward the right [40,41]. Therefore, the BDT region obtained by the non-destructive method presented here is envisaged to provide a lower limit of the macroscopic BDT curve for notched specimens. In a worked material, the BDT behaviors can be also influenced by the orientation of specimens due to the specific grain morphologies and texture induced by thermomechanical processing, since the local effective

yield stress and fracture stress can vary in the way of grain-by-grain depending on the orientation relation with the loading direction. Thus, in case of the rolled W, the types of the predominant GBs/grain that determine ductile/brittle fracture may vary as the loading direction is changed, which is statistically governed by the distribution of grains or GBs with the lowest instability limits. To address this issue, we considered various types of grains and GBs in the fracture analysis diagram and defined the BDTT as a temperature regime considering the stochastic factors. And then, we verified that the suggested method converts the orientation dependency of BDTT by additional tensile tests of various as-received specimens having different orientation (Fig. S8). The resultant temperature versus energy absorbed curves are represented in Fig 9(b). The values of measured absorption energy depended on the specimen orientation; N-T and T-R type exhibited the lower values of energy absorbed than those of N-R type, which is believed to be due to the anisotropic grain morphology in rolled structure. Nevertheless, the transition curves of all specimens showed the gradual uptrend within the estimated BDT regime determined by fracture analysis diagram, indicating that the suggested

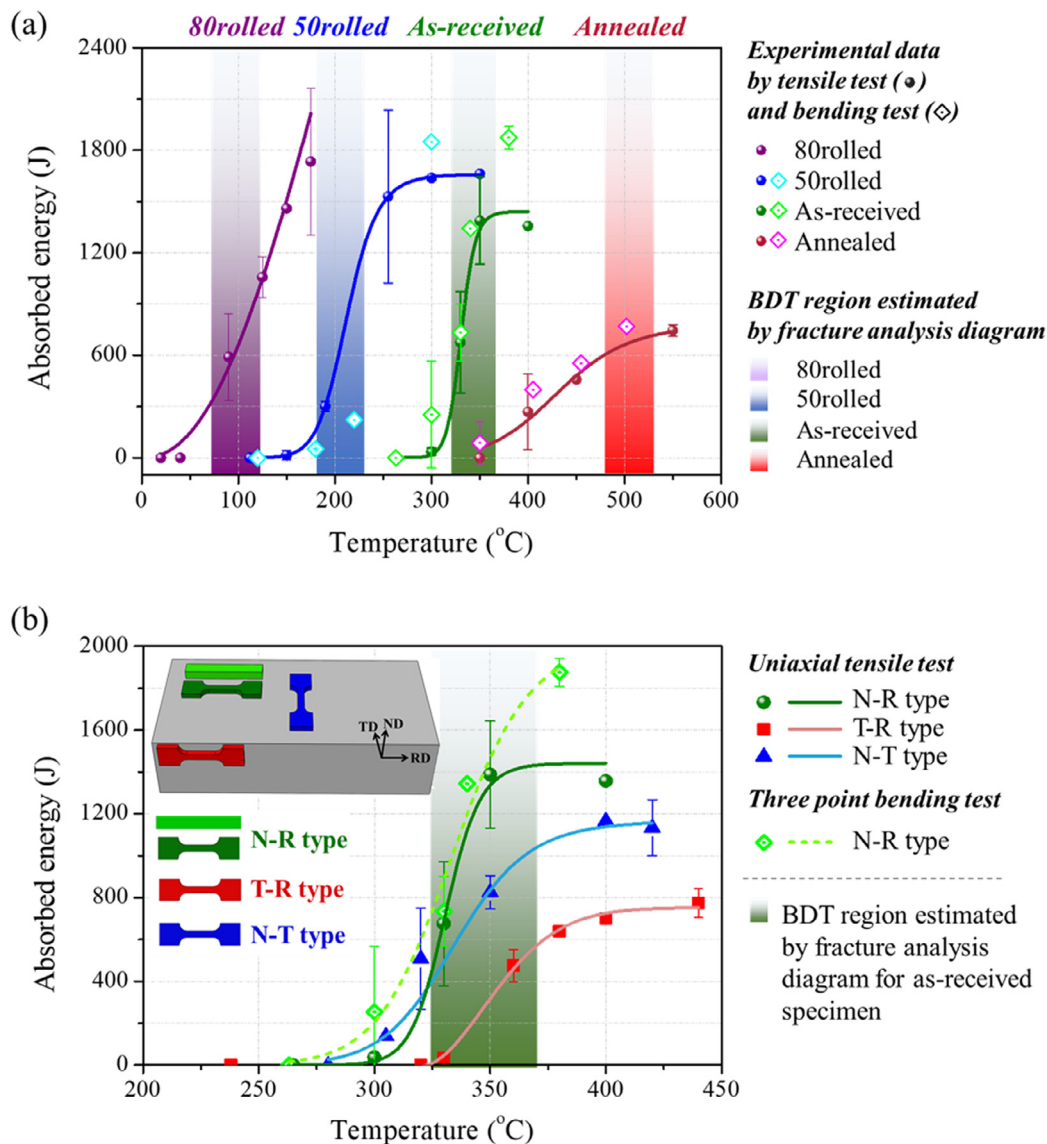


**Fig. 9.** (a) Temperature dependence of absorbed energy during tensile and bending tests for 80rolled (purple), 50rolled (blue), as-received (green), and annealed (red) specimens. Data points with the circle and diamond-shape on the solid line represent the experimental values of the tensile test and three-point bending test, respectively, corresponding to the results shown in Fig. S7. (b) Temperature dependence of absorbed energy of the as-received specimens having different orientation. The inset is the schematic representation of the specimens extracted from the as-received rolled plate in different direction. Data points with the circle, diamond, triangle, and square-shape represent the experimental values, corresponding to the results shown in Fig. S8. The shaded areas in both (a) and (b) represent the BDT regions estimated using the present fracture analysis diagram in this study.

method can cover the anisotropic response of BDT behavior in deformed W.

We can conclusively claim that it is quite reasonable to account for the macroscopic BDT behavior of pure polycrystalline W through the local mechanical characteristics of grain interiors and GBs. Such a small-scale approach will enable the new measurement of BDT behavior in pure W for particular situations that are not covered by conventional method. Although this method certainly works well for pure W, there are some limitations in its applicability. The basic concept of this analysis is focused solely on the well-known physical property of brittle W that the weak GB boundary cohesion causes the poor ductility. Thus, application of the proposed method for other materials, especially for multi-component system, can be much more challenging from the simulation side due to the lack of reliable interatomic potentials. If the material contains other factors seriously affecting cracking behav-

ior (e.g., inclusion [77], alloying element [78], multi-phases [79], impurities [80]), the fracture analysis diagrams should be reconstructed more complexly considering various microstructure factors in the target material. These challenges are waiting to be studied in future's work.

### 5.3. Microstructure dependence of BDTT in pure polycrystalline W

We observed an evident inverse correlation between the BDT region determined using the fracture analysis diagram developed and dislocation density obtained using the XRD measurement (Fig. 10), which indicated that the BDTT decreased with an increase in the dislocation density. This result is on the contrary to the general expectation of metallic materials which is accounted for hardening and degraded ductility resulting from an increase in dislocation density. [8]. Such an unusual behavior of pure W, where

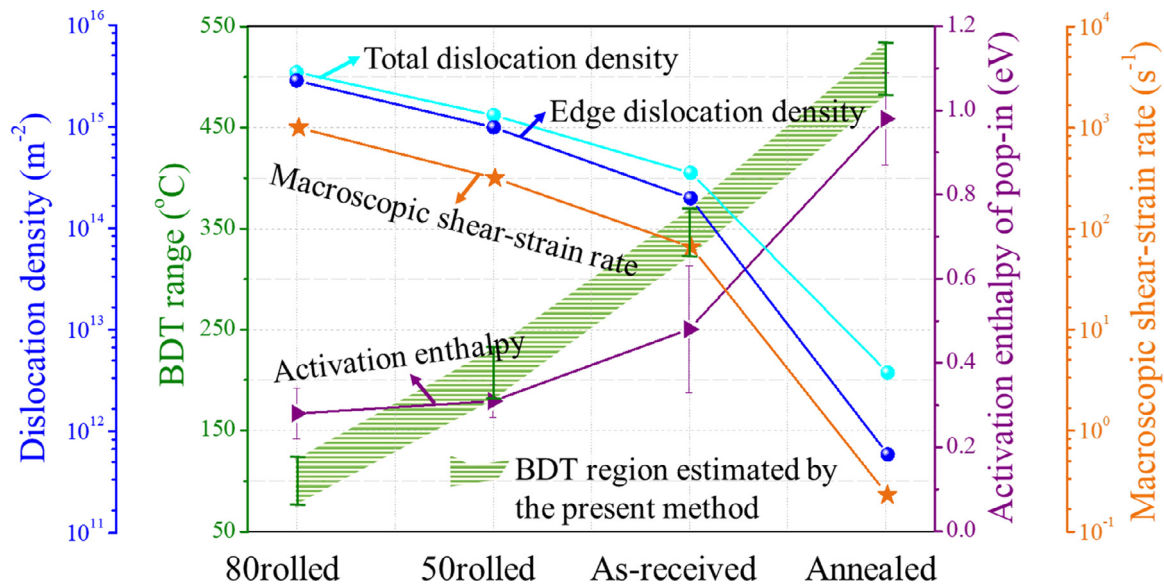


**Fig. 10.** Correlation between the dislocation density obtained by the XRD measurement, BDT region determined using the present fracture analysis diagram, activation enthalpy of pop-in determined by Eq. (7) and the shear strain rate calculated using Eq. (8) for each W specimen.

ductility can be enhanced in a cold-rolled condition and can be reduced by recrystallization, has been reported several times in previous studies [1,5–7, 27,81], but further efforts are still needed to thoroughly elucidate the BDTT reduction by thermomechanical processing. Therefore, we proceeded with a more profound analysis from two perspectives in nano- and macro-scale, focusing on the contributions of different types of dislocations, e.g., screw or edge components.

### 5.3.1. Nano-scale perspective: activation enthalpy for local plastic yielding

In a plasticity aspect while a material is under loading, increase of local stress provokes a dislocation nucleation or dislocation movement, depending on whether or not dislocation sources already exist sufficiently. To identify the controlling mechanisms of local plastic yielding, it is instructive to confirm the energy barrier for thermally activated pop-in phenomena during nano-indentation. In Section 4.2, we described the mathematical analysis of thermally activated pop-in behavior to construct the fracture analysis diagram. Based on the description developed by Mason and Schuh [31,35], we calculated the activation enthalpy from the y-intercept of linear formula [Eq. (7)] plotted in Fig. 4. The obtained values of  $Q$  are shown in Fig. 10 along with dislocation densities. It was evidently found that the energy barrier for pop-in during nano-indentation decreased as the dislocation density increased, reaching to  $\sim 0.28$  eV as for 80rolled specimen. We can expect that the pop-ins in the severely deformed W would be mainly triggered by the movement of pre-existing dislocations, since the indenter tip hardly encounters the dislocation free zone. The previous studies on plasticity of W have proven that activation enthalpy required for the glide of edge dislocation in W is 0.2–0.5 eV [82,83], while that of screw type in W is  $>1$  eV [84] because double kink pair should be antecedently formed to encourage the screw components to move. The lower values of  $Q$  in the cold-rolled specimens were comparable to that for glide of edge type dislocation, which implied that the controlling mechanism of pop-in in cold-rolled specimens was movement of edge dislocation rather than screw type. XRD analysis (Fig. 2) also found that the edge type components became dominant after severe rolling,

which demonstrated that the role of edge components is more accountable to the plastic deformation in cold-rolled W. Thus, when the cold-rolled specimens are under loading, the edge dislocations would preferentially glide near the deformation defect where the local stress rises, leading to the expansion of plastically deformed area even at low temperature.

### 5.3.2. Macro-scale perspective: macroscopic shear strain rate for plastic deformation

For bcc W to be ductile, the dislocation slip should be able to occur readily without the GB fracture until the deformation passes completely into the plastic flow. In a recent theoretical comprehension by Ren et al. [81], the contribution of pure edge or screw dislocations on the macroscopic shear strain rate ( $\dot{\gamma}_m$ ) was investigated based on the Taylor–Orowan equation. They described the  $\dot{\gamma}_m$  as a function of dislocation density at a fixed flow stress and temperature, which demonstrated that the W specimen with only edge dislocations had seven orders of magnitude higher  $\dot{\gamma}_m$  than that with only screw dislocations at the same density. By applying each density of edge and screw components in the material containing both the dislocation types, we can express the total shear strain rate on the initiation state of deformation related to whether the material yields or not:

$$\dot{\gamma}_m = b\rho_e v_e + b\rho_s v_s \quad (8)$$

Here,  $v_e$  and  $v_s$  represent the average velocities of edge and screw dislocations, respectively, as calculated by Ren et al. [81], while  $\rho_e$  and  $\rho_s$  represent the densities of edge and screw dislocations, respectively, obtained by the present XRD measurements (Section 4.1). The shear strain rate of each specimen was obtained for the same fixed flow stress (500 MPa) and temperature (200 °C), as in Ref. [81] (Fig. 10). The shear strain rate of the 80rolled specimen is estimated to be  $\sim 10^3$  s $^{-1}$ , while that of the annealed specimen drops to  $\sim 10^{-1}$  s $^{-1}$ . The results indicate that the severely rolled specimens can possess higher overall deformation rates under constant conditions where there is no change in the dislocation densities and characteristics. This is intimately linked to the previous section regarding the activation enthalpy of pop-in. In the case of cold-rolled specimens wherein the plenty of edge

dislocations are already present, the lower energy barrier for glide of edge components might result in an increase in the overall deformation rate even at relatively low temperature. This enables the material to accommodate the local deformation sufficient for macro yielding and finally undergo continuous plastic deformation before ultimate failure. On the other hand, in the annealed specimens where the mobile dislocations are insufficient, overall deformation rate is too low to cause macro yielding before GB fracture at low temperature; this is because the local shear in the annealed specimens requires either the dislocation nucleation or kink-pair formation of screw components for which the thermal energy as well as a mechanical work are needed because of their higher activation enthalpy. This explains why the BDTT of pure W specimens increased considerably after annealing in this study.

Quantitative analysis on dislocation activities addressed from nano and macroscopic perspectives have been correlated to figure out the significance of dislocation types in determining the BDTT. The enhanced ductility and resultant decrease in the BDTT of the cold-rolled specimens can now be explained by the contribution of edge dislocations that can glide faster than the screw dislocations. Evidently, there are other possible factors affecting the BDTT, such as the crystallographic texture, grain size, distributions of impurities, and low-angle GBs, developed by cold-rolling. Although further studies on the relative contributions of other factors are still required, the results presented here can contribute in deriving new design strategies for sustainable W materials by providing a deeper understanding of the unique mechanical properties of W.

## 6. Conclusion

Here, we implemented the small-scale and non-destructive characterizations to predict the macroscopic failure response so that the BDT behavior of polycrystalline pure W was investigated depending on the initial microstructure. We utilized both experimental investigation and atomistic simulation to parameterize the practical diagram for four W specimens with different microstructure (80rolled, 50rolled, as-received, and annealed). The macroscopic failure responses were then directly observed by destructive mechanical tests and correlated with the BDT estimation developed by the fracture analysis diagram in this study. Based on all finding, we ultimately provided a detailed insight into the relationship between the BDTT and dislocation densities and types in pure W. The results can be summarized as follows:

- (1) The practical fracture analysis diagram was proposed to consist of local effective yield and brittle fracture stress, which represent the resistance to dislocation activities or cracking, respectively. The BDT region is determined by analyzing the statistical significance of obtained data and specifying relevant boundary conditions in the present fracture analysis diagram.
- (2) The local effective yield stress was defined by maximum shear stresses at pop-in behaviors during nano-indentation. Based on an assumption that the pop-in behavior is a thermally activated kinetic process of dislocation nucleation or glide, we examined the relation between the temperature and maximum shear stress using the Arrhenius-type linear equation.
- (3) The fracture stresses at various temperatures were calculated by intensive MD simulations based on the newly developed interatomic potential for pure W. We confirmed that even after considering the dispersion, the overall stress for the GB fracture was significantly lower than that for the cleavage fracture in W, indicating that the decohesion of GBs was the most critical factor for the embrittlement of W.
- (4) We directly examined the failure responses at different temperatures using macroscopic uniaxial and bending tests, which

were then compared with the BDT predictions made by fracture analysis diagram. The two measures in different scales showed a good agreement, revealing that the present method can be employed as a possible tool for characterizing pure W when it requires small-scale and non-destructive experimental conditions.

- (5) We further observed an inverse correlation between the BDTT and dislocation density. Based on the correlative interpretation of activation enthalpy for pop-in and macroscopic shear strain rate, we concluded that the decreased BDTT in cold-rolled specimens was attributed to the contribution of edge dislocations that could glide faster than the screw components.

## Data availability

All data needed to evaluate the conclusions are present in the paper and/or the Supplementary Material. The raw data required to reproduce these findings are available upon reasonable request.

## Acknowledgments

This work was supported by the National Research Foundation of Korea (NRF) grant funded by the Ministry of Science, ICT (MSIT) [NRF-2020R1A5A6017701, NRF-2019M3D1A1079214, and NRF-2020R1A6A3A13076748] and the ITER Technology R&D Programme. The Institute of Engineering Research at Seoul National University also provided research facilities for this work. The authors would like to thank Ms. Nakagawa for her support in operating the high-temperature nano-indentation during the NIMS Internship Program.

## Supplementary materials

Supplementary material associated with this article can be found, in the online version, at [doi:10.1016/j.jmst.2021.07.024](https://doi.org/10.1016/j.jmst.2021.07.024).

## References

- [1] C. Ren, Z.Z. Fang, M. Koopman, B. Butler, J. Paramore, S. Middlemas, Methods for improving ductility of tungsten—a review, *Int. J. Refract. Met. Hard Mater.* 75 (2018) 170–183.
- [2] Q. Wei, L. Kecskes, Effect of low-temperature rolling on the tensile behavior of commercially pure tungsten, *Mater. Sci. Eng., A* 491 (2008) 62–69.
- [3] Q. Wei, T. Jiao, K. Ramesh, E. Ma, L. Kecskes, L. Magness, R. Dowding, V. Kazykhanov, R. Valiev, Mechanical behavior and dynamic failure of high-strength ultrafine grained tungsten under uniaxial compression, *Acta Mater* 54 (2006) 77–87.
- [4] Q. Wei, K. Ramesh, E. Ma, L. Kecskes, R. Dowding, V. Kazykhanov, R. Valiev, Plastic flow localization in bulk tungsten with ultrafine microstructure, *Appl. Phys. Lett.* 86 (2005) 101907.
- [5] J. Reiser, J. Hoffmann, U. Jäntsch, M. Klimenkov, S. Bonk, C. Bonnekoh, M. Rieth, A. Hoffmann, T. Mrotzek, Ductilisation of tungsten (W): on the shift of the brittle-to-ductile transition (BDT) to lower temperatures through cold rolling, *Int. J. Refract. Met. Hard Mater.* 54 (2016) 351–369.
- [6] Y. Oh, N. Kwak, K. Lee, W.-S. Ko, H.N. Han, Ductility enhancement of tungsten after plastic deformation, *J. Alloys Compd.* 787 (2019) 801–814.
- [7] C. Bonnekoh, A. Hoffmann, J. Reiser, The brittle-to-ductile transition in cold rolled tungsten: on the decrease of the brittle-to-ductile transition by 600K to –65°C, *Int. J. Refract. Met. Hard Mater.* 71 (2018) 181–189.
- [8] G.E. Dieter, D.J. Bacon, *Mechanical Metallurgy*, McGraw-hill, New York, 1986.
- [9] J. Lancaster, in: J. Lancaster (Ed.), *Engineering Catastrophes*, 3rd Edition, Woodhead Publishing, 2005, pp. 139–189.
- [10] J. Linke, J. Du, T. Loewenhoff, G. Pintsuk, B. Spilker, I. Steudel, M. Wirtz, Challenges for plasma-facing components in nuclear fusion, *Matter. Radiat. at Extremes* 4 (2019) 056201.
- [11] S.J. Zinkle, J.T. Busby, *Structural materials for fission & fusion energy*, *Mater. Today* 12 (2009) 12–19.
- [12] T. Zhang, H.W. Deng, Z.M. Xie, R. Liu, J.F. Yang, C.S. Liu, X.P. Wang, Q.F. Fang, Y. Xiong, Recent progresses on designing and manufacturing of bulk refractory alloys with high performances based on controlling interfaces, *J. Mater. Sci. Technol.* 52 (2020) 29–62.
- [13] R.J. Lancaster, S.P. Jeffs, H.W. Illsley, C. Argyrakis, R.C. Hurst, G.J. Baxter, Development of a novel methodology to study fatigue properties using the small punch test, *Mater. Sci. Eng., A* 748 (2019) 21–29.

- [14] W. Wang, J. Zhong, X. Zhang, T. Jiang, K. Guan, Study of estimation of ductile-brittle transition temperature using U-notched small punch test specimens, *Theor. Appl. Fract. Mech.* 108 (2020) 102627.
- [15] C. Bohnert, N.J. Schmitt, S.M. Weygand, O. Kraft, R. Schwaiger, Fracture toughness characterization of single-crystalline tungsten using notched micro-cantilever specimens, *Int. J. Plast.* 81 (2016) 1–17.
- [16] B.S. Li, T.J. Marrow, D.E.J. Armstrong, Measuring the brittle-to-ductile transition temperature of tungsten-tantalum alloy using chevron-notched micro-cantilevers, *Scr. Mater.* 180 (2020) 77–82.
- [17] T. Palacios, J.Y. Pastor, Influence of the notch root radius on the fracture toughness of brittle metals: nanostructure tungsten alloy, a case study, *Int. J. Refract. Met. Hard Mater.* 52 (2015) 44–49.
- [18] R. Carpenter, G. Paulino, Z. Munir, J.J.S.M. Gibeling, A novel technique to generate sharp cracks in metallic/ceramic functionally graded materials by reverse 4-point bending, *Scr. Mater.* 43 (2000) 547–552.
- [19] B.S. Kong, J.H. Shin, C. Jang, H.C. Kim, Measurement of Fracture Toughness of Pure Tungsten Using a Small-Sized Compact Tension Specimen, *Materials (Basel)* 13 (2020) 244.
- [20] A.K. Saxena, S. Brinckmann, B. Völker, G. Dehm, C. Kirchlechner, Experimental conditions affecting the measured fracture toughness at the microscale: notch geometry and crack extension measurement, *Mater. Des.* 191 (2020) 108582.
- [21] J.W. Morris, Stronger, Tougher Steels, *Science* 320 (2008) 1022–1023.
- [22] Y. Kimura, T. Inoue, F. Yin, K. Tsuzaki, Inverse Temperature Dependence of Toughness in an Ultrafine Grain-Structure Steel, *Science* 320 (2008) 1057–1060.
- [23] G. Grimvall, B. Magyar-Köpe, V. Ozoliņš, K.A. Persson, Lattice instabilities in metallic elements, *Rev. Mod. Phys.* 84 (2012) 945–986.
- [24] J.J.W. Morris, Z. Guo, C.R. Krenn, Y.H. Kim, The Limits of Strength and Toughness in Steel, *ISIJ Int.* 41 (2001) 599–611.
- [25] S. Giusepponi, M. Celino, The ideal tensile strength of tungsten and tungsten alloys by first-principles calculations, *J. Nucl. Mater.* 435 (2013) 52–55.
- [26] D. Roundy, C.R. Krenn, M.L. Cohen, J.W. Morris, The ideal strength of tungsten, *Philos. Mag.* 81 (2001) 1725–1747.
- [27] P. Gumbsch, J. Riedle, A. Hartmaier, H.F. Fischmeister, Controlling factors for the brittle-to-ductile transition in tungsten single crystals, *Science* 282 (1998) 1293–1295.
- [28] G.M. Pharr, W.C. Oliver, Measurement of Thin Film Mechanical Properties Using Nanoindentation, *MRS Bull.* 17 (1992) 28–33.
- [29] K. Goto, I. Watanabe, T. Ohmura, Determining suitable parameters for inverse estimation of plastic properties based on indentation marks, *Int. J. Plast.* 116 (2019) 81–90.
- [30] T.-H. Ahn, C.-S. Oh, K. Lee, E.P. George, H.N. Han, Relationship between yield point phenomena and the nanoindentation pop-in behavior of steel, *J. Mater. Res.* 27 (2012) 39–44.
- [31] C.A. Schuh, J.K. Mason, A.C. Lund, Quantitative insight into dislocation nucleation from high-temperature nanoindentation experiments, *Nat. Mater.* 4 (2005) 617–621.
- [32] H. Bei, Y.F. Gao, S. Shim, E.P. George, G.M. Pharr, Strength differences arising from homogeneous versus heterogeneous dislocation nucleation, *Phys. Rev. B: Condens. Matter* 77 (2008) 060103.
- [33] Y. Sato, S. Shinzato, T. Ohmura, S. Ogata, Atomistic prediction of the temperature- and loading-rate-dependent first pop-in load in nanoindentation, *Int. J. Plast.* 121 (2019) 280–292.
- [34] C.A. Schuh, Nanoindentation studies of materials, *Mater. Today* 9 (2006) 32–40.
- [35] J. Mason, A. Lund, C. Schuh, Determining the activation energy and volume for the onset of plasticity during nanoindentation, *Phys. Rev. B: Condens. Matter* 73 (2006) 054102.
- [36] Y.X. Ye, Z.P. Lu, T.G. Nieh, Dislocation nucleation during nanoindentation in a body-centered cubic TiZrHfNb high-entropy alloy, *Scr. Mater.* 130 (2017) 64–68.
- [37] S.-P. Wang, J. Xu, Incipient plasticity and activation volume of dislocation nucleation for TiZrNbTaMo high-entropy alloys characterized by nanoindentation, *J. Mater. Sci. Technol.* 35 (2019) 812–816.
- [38] X. Wu, Y.-W. You, X.-S. Kong, J.-L. Chen, G.-N. Luo, G.-H. Lu, C. Liu, Z. Wang, First-principles determination of grain boundary strengthening in tungsten: dependence on grain boundary structure and metallic radius of solute, *Acta Mater.* 120 (2016) 315–326.
- [39] H.-b. Zhou, J. Shuo, Y. Zhang, G.-h. Lu, Effects of hydrogen on a tungsten grain boundary: a first-principles computational tensile test, *Prog. Nat. Sci.* 21 (2011) 240–245.
- [40] R. Mishnev, N. Dudova, R. Kaibyshev, A. Belyakov, On the Fracture Behavior of a Creep Resistant 10% Cr Steel with High Boron and Low Nitrogen Contents at Low Temperatures, *Materials (Basel)* 13 (2020) 3.
- [41] F. Tioguem, M. Maziere, F. Tankoua, A. Galtier, A.-F. Gourgues-Lorenzon, Identification of ductile to brittle transition temperature by using plane strain specimen in tensile test and correlation with instrumented Charpy impact test: experimental and numerical study, *Mechanics&Industry* 19 (2018) 107.
- [42] T. Ungár, A. Borbély, The effect of dislocation contrast on x-ray line broadening: a new approach to line profile analysis, *Appl. Phys. Lett.* 69 (1996) 3173–3175.
- [43] G. Ribárik, J. Gubicza, T. Ungár, Correlation between strength and microstructure of ball-milled Al-Mg alloys determined by X-ray diffraction, *Mater. Sci. Eng., A* 387–389 (2004) 343–347.
- [44] M. Wilkens, The determination of density and distribution of dislocations in deformed single crystals from broadened X-ray diffraction profiles, *Phys. Status Solidi* 2 (1970) 359–370.
- [45] J. Ruzic, I. Watanabe, K. Goto, T. Ohmura, Nano-Indentation Measurement for Heat Resistant Alloys at Elevated Temperatures in Inert Atmosphere, *Mater. Trans., JIM* 60 (2019) 1411–1415.
- [46] B.-J. Lee, M.I. Baskes, H. Kim, Y.K. Cho, Second nearest-neighbor modified embedded atom method potentials for bcc transition metals, *Phys. Rev. B: Condens. Matter* 64 (2001) 184102.
- [47] B.-J. Lee, W.-S. Ko, H.-K. Kim, E.-H. Kim, The modified embedded-atom method interatomic potentials and recent progress in atomistic simulations, *Calphad* 34 (2010) 510–522.
- [48] G. Kresse, J. Hafner, Ab initio molecular-dynamics simulation of the liquid-metal-amorphous-semiconductor transition in germanium, *Phys. Rev. B: Condens. Matter* 49 (1994) 14251–14269.
- [49] G. Kresse, J. Furthmüller, Efficient iterative schemes for ab initio total-energy calculations using a plane-wave basis set, *Phys. Rev. B: Condens. Matter* 54 (1996) 11169–11186.
- [50] G. Kresse, J. Furthmüller, Efficiency of ab-initio total energy calculations for metals and semiconductors using a plane-wave basis set, *Comput. Mater. Sci* 6 (1996) 15–50.
- [51] P.E. Blöchl, Projector augmented-wave method, *Phys. Rev. B: Condens. Matter* 50 (1994) 17953–17979.
- [52] J.P. Perdew, K. Burke, M. Ernzerhof, Generalized Gradient Approximation Made Simple, *Phys. Rev. Lett.* 77 (1996) 3865–3868.
- [53] H.J. Monkhorst, J.D. Pack, Special points for Brillouin-zone integrations, *Phys. Rev. B: Condens. Matter* 13 (1976) 5188–5192.
- [54] F. Birch, Finite strain isotherm and velocities for single-crystal and polycrystalline NaCl at high pressures and 300°K, *J. Geophys. Res. B: Solid Earth* 83 (1978) 1257–1268.
- [55] F.D. Murnaghan, The Compressibility of Media under Extreme Pressures, *Proc. Natl. Acad. Sci. U.S.A.* 30 (1944) 244–247.
- [56] G. Henkelman, B.P. Uberuaga, H. Jónsson, A climbing image nudged elastic band method for finding saddle points and minimum energy paths, *J. Chem. Phys.* 113 (2000) 9901–9904.
- [57] G. Henkelman, H. Jónsson, Improved tangent estimate in the nudged elastic band method for finding minimum energy paths and saddle points, *J. Chem. Phys.* 113 (2000) 9978–9985.
- [58] A. Togo, F. Oba, I. Tanaka, First-principles calculations of the ferroelastic transition between rutile-type and CaCl<sub>2</sub>-type SiO<sub>2</sub> at high pressures, *Phys. Rev. B: Condens. Matter* 78 (2008) 134106.
- [59] A. Togo, I. Tanaka, Evolution of crystal structures in metallic elements, *Phys. Rev. B: Condens. Matter* 87 (2013) 184104.
- [60] B. Grabowski, L. Ismer, T. Hickel, J. Neugebauer, Ab initio up to the melting point: anharmonicity and vacancies in aluminum, *Phys. Rev. B: Condens. Matter* 79 (2009) 134106.
- [61] J.D. Honeycutt, H.C. Andersen, Molecular dynamics study of melting and freezing of small Lennard-Jones clusters, *J. Phys. Chem.* 91 (1987) 4950–4963.
- [62] A. Stukowski, Visualization and analysis of atomistic simulation data with OVITO—the Open Visualization Tool, *Modell. Simul. Mater. Sci. Eng.* 18 (2010) 015012.
- [63] S. Plimpton, Fast parallel algorithms for short-range molecular dynamics, *J. Comput. Phys.* 117 (1995) 1–19.
- [64] S. Nosé, A unified formulation of the constant temperature molecular dynamics methods, *J. Chem. Phys.* 81 (1984) 511–519.
- [65] W.G. Hoover, Canonical dynamics: equilibrium phase-space distributions, *Phys. Rev. A: At. Mol. Opt. Phys.* 31 (1985) 1695–1697.
- [66] T. Ungár, I. Dragomir, Á. Révész, A. Borbély, The contrast factors of dislocations in cubic crystals: the dislocation model of strain anisotropy in practice, *J. Appl. Crystallogr.* 32 (1999) 992–1002.
- [67] D. Hull, D.J. Bacon, *Introduction to Dislocations*, Butterworth-Heinemann, Oxford, 2001.
- [68] K.L. Johnson, K.L. Johnson, *Contact Mechanics*, Cambridge university press, Cambridge, 1987.
- [69] J. Martín, C. Pérez, in: *Safety, Reliability and Risk Analysis: Theory, Methods and Applications*, CRC Press, London, 2009, pp. 869–874.
- [70] T.H. Courtney, *Mechanical Behavior of Materials*, Waveland Press, 2005.
- [71] W.R. Tyson, R.A. Ayres, D.F. Stein, Anisotropy of cleavage in B.C.C. transition metals, *Acta Metall.* 21 (1973) 621–627.
- [72] D. Scheiber, R. Pippan, P. Puschnig, L. Romaner, Ab initio calculations of grain boundaries in bcc metals, *Modell. Simul. Mater. Sci. Eng.* 24 (2016) 035013.
- [73] B. Gludovatz, S. Wurstler, T. Weingärtner, A. Hoffmann, R. Pippan, Influence of impurities on the fracture behaviour of tungsten, *Philos. Mag.* 91 (2011) 3006–3020.
- [74] D. Rupp, S.M. Weygand, Anisotropic fracture behaviour and brittle-to-ductile transition of polycrystalline tungsten, *Philos. Mag.* 90 (2010) 4055–4069.
- [75] F. Pukelsheim, The three sigma rule, *Am. Stat.* 48 (1994) 88–91.
- [76] Y. Zhao, X. Tong, X.H. Wei, S.S. Xu, S. Lan, X.L. Wang, Z.W. Zhang, Effects of microstructure on crack resistance and low-temperature toughness of ultra-low carbon high strength steel, *Int. J. Plast.* 116 (2019) 203–215.
- [77] Y. Liu, X. Zheng, S. Osovski, A. Srivastava, On the micromechanism of inclusion driven ductile fracture and its implications on fracture toughness, *J. Mech. Phys. Solids* 130 (2019) 21–34.
- [78] K.S. Chan, Alloying effects on fracture mechanisms in Nb-based intermetallic in-situ composites, *Mater. Sci. Eng., A* 329–331 (2002) 513–522.
- [79] E. Schlangen, E.A.B. Koenders, K. van Breugel, Influence of internal dilation on the fracture behaviour of multi-phase materials, *Eng. Fract. Mech.* 74 (2007) 18–33.

- [80] P.A.T. Olsson, J. Blomqvist, Intergranular fracture of tungsten containing phosphorus impurities: a first principles investigation, *Comput. Mater. Sci* 139 (2017) 368–378.
- [81] C. Ren, Z.Z. Fang, L. Xu, J.P. Ligda, J.D. Paramore, B.G. Butler, An investigation of the microstructure and ductility of annealed cold-rolled tungsten, *Acta Mater* 162 (2019) 202–213.
- [82] A. Giannattasio, S.G. Roberts, Strain-rate dependence of the brittle-to-ductile transition temperature in tungsten, *Philos. Mag.* 87 (2007) 2589–2598.
- [83] A. Seeger, Peierls barriers, kinks, and flow stress: recent progress: dedicated to Professor Dr. Haël Mughrabi on the occasion of his 65th birthday, *Zeitschrift für Metallkunde* 93 (2002) 760–777.
- [84] H.W. Schadler, Mobility of edge dislocations on {110} planes in tungsten single crystals, *Acta Metall.* 12 (1964) 861–870.